Available online at www.sciencedirect.com

Chemical Engineering Research and Design

journal homepage: www.elsevier.com/locate/cherd

Insights by *in-situ* studies on the nature of highly-active hydrotalcite-based Ni-Fe catalysts for CO_2 methanation

Chalachew Mebrahtu[a], *Florian Krebs*[a,b], *Gianfranco Giorgianni*[c,*], *Salvatore Abate*[c], *Siglinda Perathoner*[c], *Gabriele Centi*[c], *Alexander I. Large*[d,e], *Georg Held*[d,e], *Rosa Arrigo*[d,f,**], *Regina Palkovits*[a,b,***]

[a] *Chair of Heterogeneous Catalysis and Technical Chemistry, Institute for Technical and Macromolecular Chemistry (ITMC), RWTH Aachen University, Worringerweg 2, 52074 Aachen, Germany*

[b] *Competence Center Power to Fuel, RWTH Aachen University, Schinkelstraße 2, 52062 Aachen, Germany*

[c] *University of Messina, Dpt. ChiBioFarAm, ERIC aisbl and CASPE/INSTM, Viale F. Stagno D'Alcontres 31, 98166 Messina, Italy*

[d] *Diamond Light Source, Harwell Science and Innovation Campus, OX110DE Didcot, UK*

[e] *Department of Chemistry, University of Reading, RG6 6AD Reading, UK*

[f] *School of Science, Engineering and Environment, University of Salford, M5 4WT Manchester, UK*

ARTICLE INFO

Article history:
Received 20 December 2022
Received in revised form 10 March 2023
Accepted 14 March 2023
Available online 17 March 2023

Keywords:
Ni-Fe hydrotalcite
Basic sites
CO_2 methanation
APXPS
DRIFTS

ABSTRACT

Designing CO_2 methanation catalysts that meet industrial requirements is still challenging. We report Ni-Fe hydrotalcite-derived catalysts with a wide range of Ni and Mg loadings showing that an optimised composition with $Ni_{0.4}$ gives a very high CO_2 conversion rate of 0.37 mmol/g_{cat}/s at 300 °C. This catalyst is studied by *in-situ* APXPS and NEXAFS spectroscopies and compared with the other synthesised samples to obtain new mechanistic insights on methanation catalysts active for low-temperature (300 °C) methanation, which is an industrial requirement. Under methanation conditions, *in-situ* investigations revealed the presence of metallic Ni sites and low nuclearity Ni-Fe species at x^L_{Ni} (Ni loading) = 21.2 mol%. These sites are oxidised on the low Ni-loaded catalyst (x^L_{Ni}= 9.2 mol%). The best CO_2 conversion rate and CH_4 selectivity are shown at intermediate x^L_{Ni} (21.2 mol%), in the presence of Mg. These superior performances are related to the high metallic surface area, dispersion, and optimal density of basic sites. The TOF_{CO_2}(turnover frequency of CO_2 conversion) increases exponentially with the fractional density of basic to metallic sites (X_B) from 1.1 s^{-1} (x^L_{Ni}= 29.2 mol%) to 9.1 s^{-1} (x^L_{Ni}= 7.6 mol%). It follows the opposite trend of the CO_2 conversion rate. *In-situ* DRIFTS data under methanation conditions evidence that the TOF_{CO_2}at high X_B is related to the presence of a formate route which is not predominant at low X_B (high x^L_{Ni}). A synergistic interplay of basic and metallic sites is present. This contribution provides a rationale for designing industrially competitive CO_2 methanation catalysts with high catalytic activity while maintaining low Ni loading.

* Corresponding author.
** Corresponding author at: Diamond Light Source, Harwell Science and Innovation Campus, OX110DE Didcot, UK.
*** Corresponding author at: Chair of Heterogeneous Catalysis and Technical Chemistry, Institute for Technical and Macromolecular Chemistry (ITMC), RWTH Aachen University, Worringerweg 2, 52074 Aachen, Germany.
E-mail addresses: gianfranco.giorgianni@unical.it (G. Giorgianni), r.arrigo@salford.ac.uk (R. Arrigo), palkovits@itmc.rwth-aachen.de (R. Palkovits).

https://doi.org/10.1016/j.cherd.2023.03.026

1. Introduction

The electrification of chemical production and enhancing carbon circularity by reusing CO_2 are key aspects of the ongoing energy transition (Centi and Perathoner, 2022a, 2022b; Mustafa et al., 2020; Navarrete et al., 2017; Papanikolaou et al., 2022a; Perathoner et al., 2021; Price et al., 2021). The so-called power-to-gas (P2G) technology is part of those necessary to enable storing intermittent renewable energy using CO_2 as feedstock to produce synthetic natural gas (SNG) *via* the Sabatier reaction (Blanco and Faaij, 2018; Giglio et al., 2018; Götz et al., 2016; Hussain et al., 2021; Salomone et al., 2019; Su et al., 2016).

The Sabatier reaction also referred to as CO_2 methanation, is favoured at high pressure and low temperature. However, kinetic limitations hinder achieving a high reaction rate and selectivity to methane at the low temperatures required to operate this exothermic reversible reaction at a more favourable equilibrium (Papanikolaou et al., 2022b). Catalytic systems based on noble and non-noble metals such as Fe, Ru, Co, Rh, Ir, Ni, Pd, and Pt supported on different metal oxides (Al_2O_3, SiO_2, ZrO_2, CeO_2, TiO_2) were investigated for this reaction (Aziz et al., 2014; Garbarino et al., 2014; Nematollahi et al., 2015; Tsiotsias et al., 2022; Wang et al., 2022; Yang Lim et al., 2016; Zhou et al., 2016). The use of earth-abundant-based catalysts, however, is preferable from a sustainability perspective.

Ni-based catalysts offer good catalytic activity and a competitive price but suffer from deactivation (Aziz et al., 2015; Ding et al., 2016; Muroyama et al., 2016). Catalyst design strategies for improving catalytic performance involve controlling the support's active metal dispersion, metal loading, and surface chemistry (Feng et al., 2009; Lima et al., 2020; Tada et al., 2021; Wang et al., 2012; Younas et al., 2016; Zhao et al., 2010). A high loading is needed to achieve high activity (Lu and Kawamoto, 2013; Wang et al., 2016).

In commercial methanation catalysts, high-loading Ni catalysts (Ni loadings ≥ 50 wt%) are usually prepared *via* co-precipitation. However, using such a high Ni loading, necessary for low-temperature activity, is not ideal for both cost and stability. Recently, hydrotalcite-derived catalysts have gained great attention due to their structural architecture and compositional flexibility (Fan et al., 2014; Feng et al., 2015), which allow tuning surface properties (*i.e.* acid-base and reducibility) (Sun et al., 2021) and obtain a high metal dispersion (Xu et al., 2015). The basic and acidic properties of the metal oxide support in the final catalyst can be tailored by changing the Mg and Al ratio (Climent et al., 2004; Liu et al., 2016).

Regarding the use of hydrotalcite-derived catalysts for CO_2 methanation, properties such as the basicity (He et al., 2014; Wierzbicki et al., 2017), the effect of the Ni amount (Wierzbicki et al., 2017), the morphology and size of the Ni crystallites (Gabrovska et al., 2011), the synthesis conditions (Abate et al., 2016; Gabrovska et al., 2011) and long term stability (Bette et al., 2016) have been investigated. These studies demonstrate the suitability of hydrotalcite-derived catalysts for CO_2 methanation. However, there are still many questions to be addressed. Among the hydrotalcite-derived Ni-based catalysts with high metal loading, Ni-Fe bimetallic catalysts are emerging as promising systems in CO_2 methanation (Abate et al., 2016; He et al., 2014; C. Mebrahtu et al., 2018b). Fe species have a protective effect on metallic Ni, preventing either its hydroxylation (Mebrahtu et al., 2019) or poisoning by CO (Serrer et al., 2021). By alloying with Ni or forming a Ni-Fe(O_x) interface (Mutz et al., 2017), Ni or metal-oxide interfacial sites reduce easier (Winter et al., 2018; Yan et al., 2019). The exsolution of Fe to the surface as Fe^{2+} provides synergistic active sites (Burger et al., 2020). Multiple effects are thus present, although their effective role has not been proven by *in-situ* studies, particularly on samples with industrially relevant performances active in low-temperature operations.

We recently reported high methanation activity and selectivity for Ni-Fe-Mg-Al hydrotalcite-derived systems with uniformly distributed Ni nanoparticles, outperforming commercial Ni catalysts (Mebrahtu et al., 2018b). We also showed that incorporating Fe into Ni-Mg-Al hydrotalcite produces Lewis basic sites of different strengths, raising the question of whether these sites can be used as activity descriptors in CO_2 methanation (Mebrahtu et al., 2018b). The type and amount of basic sites available on the catalyst surface were reported as the predominant structural features affecting CO_2 methanation (Aldana et al., 2013; Korhonen et al., 2008; Pan et al., 2014b; Zamani et al., 2015). Pan et al. (2014b) indicated by CO_2-TPD that only medium basic sites are responsible for the higher activity of Ni/CeO_2-ZrO_2 compared to Ni/Al_2O_3. In contrast, He et al. (2014) obtained an enhanced CO_2 conversion and CH_4 selectivity by introducing extra-strong basic sites using KOH on Ni-Al_2O_3-Hydrotalcite. However, the main issue is that the presence of CO_2 feed changes the surface basicity character during catalytic operations due to CO_2 chemisorption. Thus, an *in-situ* study would be necessary to obtain better mechanistic insights (Arrigo et al., 2020, 2018, 2022; Giorgianni et al., 2020; Law et al., 2015; Vogt et al., 2019, 2018). However, these studies provide reliable and relevant mechanistic insights only when a careful selection of suitable catalysts to investigate is made. In addition, as chemisorption strongly depends on the reaction's temperature, studies on active catalysts only at higher temperatures (> 400–450 °C) do not provide reliable indications on the mechanistic aspects of those operating at around 300 °C.

This study combines an accurate selection of structurally tailored catalysts and complementary *in-situ* characterisation methods to clarify mechanistic insights and develop a nanostructure/activity relationship for the methanation reaction. With respect to the literature, it provides for the first time indications by both *ex-situ* and *in-situ* methods on the catalyst dynamics and mechanistic aspects of a highly active catalyst operating at a low temperature (300 °C) as requested from an industrial perspective. In contrast, literature data are only *ex-situ* or made for much higher temperature operations and less active catalysts.

A series of Ni-Fe-Mg-Al hydrotalcite-derived catalysts with different densities of basic sites and active metal loading were prepared by modulating the Ni-Fe/Mg-Al ratio. The Mg/Al ratio was changed to tailor structural properties while the Ni/Fe ratio was maintained constant. The catalysts were characterised using a combination of physicochemical methods to provide both *ex-situ* and *in-situ* indications on the nature of the catalysts and structure-activity relationships. Powder X-ray diffraction (PXRD), H_2 temperature-programmed reduction (H_2-TPR), CO_2-temperature programmed desorption (CO_2-TPD), scanning electron microscopy (SEM), and CO-chemisorption, *in-situ* ambient pressure X-ray

photoelectron spectroscopy (APXPS), near-edge X-ray absorption fine structure spectroscopy (NEXAFS) and diffuse reflectance infrared Fourier Transform spectroscopy (DRIFTS) methods were used in this study.

2. Experimental section

2.1. Catalysts preparation

The catalysts were prepared by coprecipitation method, as detailed in previous work (Mebrahtu et al., 2018b, 2019), from Ni, Fe, Mg, and Al precursors to obtain catalysts with the desired metallic molar fractional compositions (x^d_M, with M = Ni, Fe, Mg, Al) as summarised in Table 1. As previously determined, the Ni/Fe ratio was fixed to the optimised value of 10 (Mebrahtu et al., 2018b; Mebrahtu et al., 2019). The molar Mg/Al ratio was tailored between 0 and 4.

The designed, oxygen-free Ni molar fraction (x^d_{Ni}) was varied between 0 and 0.75, corresponding to a change in the x^d_{Mg} between 0.75 and 0 ($x^d_{Mg} = 0.75 - x^d_{Ni}$, Table 1). The achieved metallic loadings are reported in the results and discussion section.

2.2. Structural characterisations

The X-ray diffraction (XRD) patterns were measured using a D2-Phaser instrument (Bruker) for the catalysts at the different synthesis steps: a) as prepared and dried, b) after calcination and, c) after reduction. Reduced catalysts were prepared *ex situ*, using a tubular furnace, in H_2 at 600 °C for 2 h, to mimic the reduction procedure employed before each catalytic activity test. All the catalysts were measured using a standard copper X-ray tube, operated at 30 kV and 40 mA (Cu-K_α radiation, $\lambda = 1.54178$ Å), within a 2θ range of 10–90° and a time per step of 0.5 s

An EAGLE μ-Probe X-ray fluorescence diffractometer (EDAX Inc.) was used to measure the molar composition of the as-prepared catalysts.

N_2-physisorption isotherms of the calcined and *ex situ* pre-reduced catalysts (–196 °C) were measured with an Autosorb IQ2 (Quantachrome Instruments). Before each analysis, the samples were outgassed at 200 °C under vacuum for 16 h. The specific surface area was calculated by using the standard multipoint BET method. The total pore volume was calculated at p/p° of 0.97.

A ChemBET Pulsar TPR/TPD/TPO (Quantachrome Instruments), equipped with a TCD detector, was used to measure temperature-programmed reduction profiles of the calcined catalysts. For each experiment, 50 mg of catalyst was outgassed in Helium flow at 200 °C for 1 h. Then, the temperature of the oven was lowered to 100 °C. After stabilisation of the TCD signal, the catalysts were subjected to a thermal treatment at a rate of 10 °C.min^{-1} in the temperature range 100–1000 °C and in a mixture of 5% H_2/Ar.

SEM micrographs were acquired using a DSM 982 Gemini (Zeiss) scanning electron microscope (SEM), operating with an acceleration voltage of 3 kV. The samples were C-coated before the SEM investigation using a sputter-coater.

An AutoChem-II (Micromeritics), equipped with a TCD detector, was used to measure a) the CO_2 temperature-programmed desorption profiles (CO_2-TPD) of the reduced catalysts and b) their Metallic Surface Areas (MSA) by CO pulse chemisorption. Before both analyses, the calcined catalysts were reduced *in-situ* in H_2 (50 mL/min) at 600 °C (10 °C/min) for 2 h. Then, each sample was treated at 300 °C for 1 h in He flow to clean the surface. CO pulse chemisorption was measured at 40 °C in He flow (50 mL/min) using a 0.5 mL calibrated loop fed with a 10% CO/He mixture. In the case of CO_2-TPD experiments, the catalysts were cooled down to 80 °C after the treatment at 300 °C in He flow, then CO_2 (30 mL/min) adsorption was performed for 1 h, then the sample was kept in a He flow (30 mL/min) for another 1 h to clean physisorbed CO_2 from the surface, and cooled down to 50 °C. Finally, CO_2-TPD profiles were obtained between 50 and 800 °C, using a ramping rate of 5 °C/min.

The obtained CO_2-TPD profiles were fitted using 4 or 5 Gaussian functions. For an easier comparison among the measured catalysts, the fitted areas for each catalyst ($A_{X,A,Cat}$, x: peak number) were divided by the total area of the most basic catalyst ($A_{Total,MBC}$) as given in Eq. (1), and indicated as relative ($B_{X,A}$) and total density of basic sites ($B_{Total,A}$, Eq. 2).

$$B_{X,A,Cat} = \frac{A_{X,A,Cat}\,[mV\cdot \min]}{A_{Total,MBC}\,[mV\cdot \min]} \quad (1)$$

$$B_{Total,A} = \sum_{X=1}^{X=5} B_{X,A},\ 0 < B_{Total,A} < 1 \quad (2)$$

Metallic surface areas (MSA, m^2/g), and metal dispersion measured by CO-chemisorption were calculated using the assumption of a CO/Metal = 1. The last assumption is reasonable considering the low CO chemisorption temperature employed. The molar amount of CO per gram of catalyst was used for calculating the TOF_s. The catalysts were normalised

Table 1 – Sample notations and nominal compositions.

#	Catalyst Name	[[a]	[[a,b]	[[a,c]	[[a,d]	Ni/Fe[e]	Mg/Al[e]
1	Ni_0	0	0	0.750	0.250	-	3
2	$Ni_{0.12}$	0.120	0.012	0.630	0.238	10	2.6
3	$Ni_{0.2}$	0.200	0.020	0.550	0.230	10	2.4
4	$Ni_{0.4}$	0.400	0.040	0.350	0.210	10	1.7
5	$Ni_{0.6}$	0.600	0.060	0.150	0.190	10	0.8
6	$Ni_{0.75}$	0.750	0.075	0	0.175	10	0

[a] x^d_M represents the nominal, metallic molar fractional composition of the catalysts without considering the amount of oxygen. This is used as a base for calculating the precursors' amount for the coprecipitation; $x^d_{Ni} + x^d_{Fe} + x^d_{Mg} + x^d_{Al} = 1$

[b] $x^d_{Fe} = 0.1x^d_{Ni}$

[c] $x^d_{Mg} = 0.75 - x^d_{Ni}$

[d] $x^d_{Al} = 0.25 - 0.1x^d_{Ni}$

[e] Ni/Fe and Mg/Al, molar ratios (mol/mol)

to the molar amount of CO of the highest CO adsorption per gram of catalyst (MC, see Eq. 3), for an easier comparison.

$$M = \frac{n_{CO,Cat}\,[mmol \cdot g^{-1}]}{n_{CO,MC}\,[mmol \cdot g^{-1}]} \quad (3)$$

To describe the reaction, we found it useful to introduce the surface fraction of basic sites (X_B, Eq. 4), considering the total density of basic and metallic sites.

$$X_B = \frac{B_{Total,A}}{B_{Total,A} + M},\ 0 < X_B < 1 \quad (4)$$

A Tecnai F20 (FEI) high-resolution transmission electron microscope (HRTEM), operating with an acceleration voltage up to 200 kV and equipped with a Gatan GIF 2000 energy filter, EDX (EDAX), and a HAADF detector, was used to acquire the micrographs and EDX mappings of the $Ni_{0.2}$ and $Ni_{0.4}$ catalysts after reduction at 600 °C under H_2.

A Bruker VERTEX 70 spectrometer was equipped with an MCT detector, and a Praying Mantis cell (Harrick; ϕ.h: 4.53 mm; internal volume: 47.7 mm^3) was used for *in-situ* DRIFTS experiments of the prepared catalysts. The catalysts were pre-reduced *ex-situ* at 600 °C using the above-reported procedure and transferred to the DRIFTS cell using a glove box without air exposure. An additional *in-situ* reduction treatment at 400 °C in H_2 (20 mL/min of H_2 for 30 min) was performed in the DRIFTS cell to minimise the presence of surface oxidised species eventually formed during the sample transfer. Subsequently, the catalysts were cooled down to the target temperature under N_2 flow (20 mL/min), and background spectra were recorded (64 scans from 1000 to 4000 cm^{-1}; resolution of 4 cm^{-1}). CO_2 adsorption experiments (CO_2-DRIFTS) were performed at 200, 300, and 400 °C, using a 10% CO_2/N_2 (50 mL/min) mixture with stepwise spectra collection (1 min interval). The *in-situ* CO_2 methanation experiments (M-DRIFTS) were performed using freshly pre-reduced catalysts at 200, 300, and 400 °C, feeding a mixture of 50 mL/min ($CO_2/H_2/N_2$ = 1/4/1 v/v). The temperature was held constant for 30 min, and the spectra were continually recorded at each temperature, with an acquisition time of 3 min per spectrum. During CO_2 adsorption and methanation experiments, to clean the catalyst surface and remove the effect of pre-adsorbed CO_2, temperature ramps were performed under N_2 flow, and background spectra were collected at each temperature.

The APXPS and NEXAFS experiments were performed at the B07 beamline (Giorgianni et al., 2020) at the UK synchrotron facility Diamond Light Source. The exit slit (ES) was set to 0.5 µm x 0.04 µm and the fix focus constant (cff) to 2.0 (cff = cos(α)/cos(β)). A thin layer of the calcined catalysts was drop-casted onto Au-coated silicon wafers to circumvent charging issues. The XPS Ni2p, C1s, and O1s core levels were measured using an X-ray excitation energy corresponding to an electron kinetic energy (KE) of 450 eV. The pass energy (Ep) was set to 20 eV. After each core level measurement, the Fermi edge was measured at the same excitation energy and used to calibrate the energy scale of the spectra. Only the relative distribution of the species will be discussed under the different ambient conditions; therefore, no further normalisation of the signal intensity in count per second (CPS) was carried out to take into account the different scattering of electrons in the gas phase, which depends on the gas-phase composition.

Electron Yield (EY) NEXAFS spectra were recorded with an analyser setting of 50 eV pass energy (Ep) and electron kinetic energy (KE) of 780 eV, 600 eV, 400 eV, and 240 eV for Ni L-, Fe L-, O K- and C K-edges, respectively.

The spectra of the $Ni_{0.2}$, $Ni_{0.4}$, and $Ni_{0.6}$ catalysts were first measured on the calcined samples at room temperature and UHV conditions. The samples were then reduced *in-situ* at 600 °C using 50 – 70 mbar H_2 for 3 h. Next, the samples were measured in an H_2 environment (4 mbar, 300 °C; if not otherwise stated). The spectra after pre-reduction, the catalysts were measured in H_2 (Hy1, 300 °C, 4 mbar) and methanation conditions (M1, H_2:CO_2 = 4, 300 °C, 5 mbar). $Ni_{0.2}$ was measured in CO_2 after Hy1 (Cd1, 3 mbar, 300 °C). Instead, after Hy1 and M1, $Ni_{0.4}$ was also further treated and measured in H_2 (Hy2, 4 mbar, 300 °C) to restore the degree of reduction and then during a second methanation cycle (M2). During these experiments, the gases were introduced using leak valves, and the pressure was stabilised before the spectroscopic measurements. A capillary positioned close to the catalyst surface allows the feeding of the gases directly onto the catalyst's surface. An online MS is positioned at the 1st pumping stage and allows the analysis of the reactive atmosphere above the catalyst's surface.

The Ni2p and C1s core level envelopes were fitted using Casa XPS software after subtracting a U2 Tougaard background. The Ni2p core level spectra fitting procedure was developed in a previous contribution and applied here (Giorgianni et al., 2020).

The C1s core level spectra were fitted using a peak with GL (30) line shape and 1.6 full widths at half maximum (FWHM). The binding energy of the components was constrained to the same values in every spectrum. The NEXAFS spectra were compared after linear background subtraction and edge-jump normalisation.

2.3. Catalysts performance testing

20 mg of calcined catalysts, diluted with 500 mg SiC (250–500 µm mesh), were tested in a fixed-bed quartz tubular reactor (internal diameter: 4 mm) at atmospheric pressure and 300 °C in differential conditions. Before each test, all the catalysts were reduced *in-situ* with 50 mL/min pure H_2 for 2 h at 600 °C and cooled to 300 °C under N_2 flow. The reduction temperature is fixed to 600 °C for all catalysts based on the reduction degrees obtained and similar treatment conditions with the *in-situ* APXPS and NEXAFS measurements. Then, a mixture of H_2, CO_2, and N_2 (in the volume ratio of 76%, 19%, and 5%, respectively) was fed into the reactor at a gas hourly space velocity (GHSV) of 66,845 h^{-1} For a fair comparison, the catalyst bed temperature is recorded in a temperature range from 240 °C up to 310 °C, and interpolation was used to obtain consistent activity data at 300 °C for comparison. The lower temperature limit was chosen to avoid nickel loss due to nickel carbonyl formation. The upper-temperature limit was chosen to obtain activity data under differential conditions for conversions below 15% to avoid transport limitations. The reactor outlet was connected to Agilent 7890B gas chromatograph equipped with TCD and FID detectors to measure the reaction products online. Carbon balances were always greater than 97%.

The rates of conversion and production for each component per mass of catalyst ($r_s^m\,[mmol \cdot s^{-1} \cdot g^{-1}]$, s = CO_2, CO, CH_4) were calculated by Eqs. 5 – 7.

$$r_{CO_2}^m = \dot{n}_{CO_2} \cdot X_{CO_2} \cdot m_{Cat}^{-1} \quad (5)$$

$$r^m_{CO} = r^m_{CO_2} \cdot S_{CO} \quad (6)$$

$$r^m_{CH_4} = r^m_{CO_2} \cdot S_{CH_4} \quad (7)$$

Whereby $\dot{n}_{CO_2}$ is the molar flow rate of CO_2, $[mmol \cdot s^{-1}]$, $X_{CO_2}$is the fractional conversion of CO_2 and, $m_{Cat}[g]$ the amount of catalyst in the reactor; S_{CO} and S_{CH_4} are the fractional selectivity toward CO and CH_4.

The rates of conversion and production for each component are normalised by the molar amount of Ni and Fe ($r^n_s[s^{-1}]$) were calculated by Eq. (8), using the molar amounts of Ni and Fe per gram of catalyst measured by XRF $(n_{Ni} + n_{Fe})[mmol \cdot g^{-1}]$.

$$r^n_s[s^{-1}] = r^m_s \cdot (n_{Ni} + n_{Fe})^{-1} \quad (8)$$

Finally, turnover frequencies for each component ($TOF_s[s^{-1}]$, Eq. 9) were calculated by the ratios of the rate of consumption and formation for each component per gram of catalysts (r^m_s, Eqs. 5–7) and the molar amount of chemisorbed CO per mass of catalyst ($d_{CO}[mmol \cdot g^{-1}]$), as measured by CO pulse chemisorption.

$$TOF_s = \frac{r^m_s}{d_{CO}} \quad (9)$$

3. Results

This study focuses on an *in-situ* mechanistic study in CO_2 methanation of an industrial-relevant Ni-Fe hydrotalcite-derived catalyst. This objective requires properly identifying a suitable sample and defining structural, surface and reactivity trends in a homogeneous set of samples to correlate the mechanistic indications to these properties. For this reason, the initial part of this work will define these aspects. However, most of the data and part of the discussion are reported in the Supplementary Information to focus the manuscript. The indication S in the Figures and Tables indicates that they are reported in the Supplementary Information.

3.1. *Structural characterisation of the catalysts*

The samples, after coprecipitation and drying, are characterised by a crystalline hydrotalcite phase (Fig. S1a and description therein), which transforms upon calcination into face-centred cubic (fcc) NiO and MgO in the periclase phase (Fig. S1b).

The transformation of the hydrotalcite phase is consistent with the morphological characterisation by SEM in Fig. S2 showing platelet-like particles for the dried Ni_0 and $Ni_{0.12}$ samples and a rosette-like morphology typical of hydrotalcites (Abelló et al., 2005; Vaccari, 1998; Wang et al., 2010) for the dried $Ni_{0.4}$ and $Ni_{0.6}$ samples. These morphologies are retained after the calcination step (Fig. S3), in agreement with Mette et al. (2014). Literature data indicate that a solid solution of $Ni_xMg_{1-x}O$ forms when the Ni molar fraction ranges between 0.12 and 0.75 (Arena et al., 1996; Matteuzzi et al., 1994). MgO and $MgAl_2O_4$ spinel phases are evident only in the absence of Ni. After the reduction treatment of the catalysts at 600 °C in pure H_2, only reflections associated with metallic Ni and periclase-like fcc phases are observed in the diffractograms for nickel-containing samples (Fig. S1c) (Gazzano et al., 1997; Lucrédio et al., 2007; Matteuzzi et al., 1994; Rebours et al., 1994).

Due to the absence of other crystalline phases, Al^{3+} ions are expected to be either in an amorphous phase or incorporated into the MgO lattice, leading to a periclase-type phase $(Ni, Al)_xMg_{1-x}O$ in which Both Ni^{2+} and Al^{3+} partially substitute Mg^{2+} (Lucrédio et al., 2007; Matteuzzi et al., 1994; Rebours et al., 1994). Moreover, the absence of reflections due to segregated Fe phases suggests the formation of stable and highly dispersed Fe, in the $Ni(Mg, Al)O_x$ matrix or into the metallic Ni phase. A more detailed discussion of the XRD results is provided in the Supporting Information.

The achieved Ni and Fe molar fractional compositions on the prepared catalysts, as measured by XRF (x^m_{Ni}, x^m_{Ni}, Table S1) are close to the theoretical value; in contrast, significant deviations are observed in the case of Mg and Al at higher x^d_{Ni}. The Ni loading was reported as metallic molar fractions (x^L_M). It ranges between 0 and 0.376 (Table S1).

Pure calcined MgO presents the lowest specific BET surface area (S_{BET} = 40 m²/g, Table S1) and pore volume (V_p = 0.13 cm^3/g). After the reduction pre-treatment under H_2, the S_{BET} and V_p of MgO increase to 123 m^2/g and 0.3 cm^3/g, respectively. S_{BET} of the calcined catalysts increases linearly with the Mg/Al ratio from 174 m^2/g to 234 m^2/g for the $Ni_{0.75}$ and $Ni_{0.2}$, respectively (Table S1 and Fig. S4a). At the same time, the total pore volume (V_p) increases linearly from 0.48 to 0.73 cm^3/g when the Al loading increases from 6.4% to 14% (x^L_{Al}, Fig. S4b), with no correlation between V_p and the Mg/Al ratio (Fig. S4c).

After the reduction treatment, S_{BET} of the catalysts increases linearly with the Mg/Al ratio (Table S1 and Fig. S4a). However, compared with the calcined catalysts, it decreases for all the samples, with an S_{BET}-loss increasing at low Mg/Al ratios. Besides, the V_p of the reduced catalysts decreases, compared to calcined ones, and no correlation with Al loading is observed (Fig. S4b). At the same time, a linear increase as a function of the Mg/Al ratio is observed (Fig. S4c). The observed textural differences among the calcined samples are a consequence of the different particle morphologies evidenced in the SEM micrographs (Figs. S2 and S3). Notably, catalysts showing flake-like morphology ($Ni_{0.12}$ and $Ni_{0.2}$) show larger S_{BET} than samples with compact particles and no evident platelet-like morphology (*i.e.* $Ni_{0.4}$ – $Ni_{0.75}$), highlighting the effect of composition on morphology and textural properties (Ferreira et al., 2019; González-Cortés et al., 2007; Zhu et al., 2016). The observed losses in S_{BET} and V_p after reduction with H_2 are related to the structural and pore network rearrangements, minimised by increasing the Mg/Al ratio.

A standard reduction treatment (pure H_2 flow for 2 h at 600 °C) followed by cooling to 300 °C under N_2 flow was applied to all the samples, including for *in-situ* APXPS and NEXAFS measurements, to achieve comparable results. The reduction temperature was selected after preliminary tests to avoid a large decrease in the surface area and drastic sintering of the Ni crystallites.

The calcined catalysts' reducibility, as determined by H_2-TPR, increases with the Ni loading (Fig. S5). While no reduction peak is observed for Ni_0, the other catalysts exhibit a broad high-temperature reduction peak, with the onset and a peak maximum shifting from 766 and 905 °C to 493–593 °C as Ni loading increases, respectively, indicating an enhancement of the reducibility. The high-temperature peak is previously assigned to Ni^{2+} reduction within the lattice of a Ni-Mg-Al solid solution (Liu et al., 2014). Besides, $Ni_{0.12}$ and $Ni_{0.2}$ present a weak H_2 consumption peak at 450 °C, attributed to

the reduction of NiO at the outermost layer of the support (Liu et al., 2014; Parmaliana et al., 1990). The reduction profile of pure NiO, investigated in a previous paper as a benchmark (Abate et al., 2016), showed a sharp reduction peak at 383 °C and a small shoulder at 283 °C, in agreement with the literature (Garbarino et al., 2014). The improved reducibility with increasing Ni loading can be related to the exsolution of Ni from the spinel phase at high Ni/Al ratios (Liu et al., 2014), leading to the formation of small supported NiO crystallites. Fe loading favours this process (Parmaliana et al., 1990).

CO_2-TPD of the pre-reduced catalyst is applied to determine the strength and density of basic sites on the pre-reduced catalysts at 600 °C. All the obtained CO_2-TPD profiles (Fig. S6) were fitted with four Gaussian peaks except for the $Ni_{0.2}$ catalyst, which presents an additional peak at 525 °C. Overall, in the case of Mg-Al mixed oxides, basic sites are usually classified into three classes: weak (93–154 °C, $B_1 - B_2$), medium (200–230 °C, B_3), and strong (283–326 °C, $B_4 - B_5$), which could be attributed to bicarbonates, unidentate and bidentate carbonates, respectively (Di Cosimo et al., 2000, 1998; Silva et al., 2010; Veloso et al., 2008). However, the partial oxidation of Ni after CO_2 adsorption can also lead to CO_2 dissociation and desorption of minor amounts of CO during the temperature ramp, as it will be shown later by CO_2-DRIFTS. The fitting of the CO_2-TPD profiles (Fig. S6, Table S2) indicates that the medium basic sites (B_3) are predominant in all the analysed samples. Moreover, the total number of basic sites ($B_{A,\ Total}$) decreases with Ni-Fe loading by 58%, passing from $Ni_{0.2}$ to $Ni_{0.75}$ (Table S2).

The metallic surface area (MSA), measured by CO chemisorption, shows a maximum value for the $Ni_{0.6}$ catalyst (Table 2). The $Ni_{0.12}$ catalyst shows the lowest MSA, while $Ni_{0.75}$ and $Ni_{0.2}$ present similar MSA values. The dispersion increases with Ni loading (decreasing Mg loadings) in the series $Ni_{0.12} - Ni_{0.6}$, while, in the absence of Mg, it decreases for $Ni_{0.75}$ (Fig. S7, Table 2). The catalysts' reduction degree, measured by H_2-TPR after pre-reduction in H_2 at 600 °C, increased with the Ni loading from 78% to 92% (Table 2). In agreement, the lower reduction degree measured at low Ni loadings is mainly related to oxidised Ni within the bulk of the catalysts, inaccessible for catalysis. Although $Ni_{0.6}$ presents a lower Ni loading than $Ni_{0.75}$, its superior MSA and dispersion can be promoted by Mg at low loadings. We postulate that Mg, in the $Ni_{0.6}$ catalyst (Mg/Al ratio of 1.59 mol/mol), as compared to $Ni_{0.75}$ (Mg/Al: 0 mol/mol), can replace Ni for the formation of $Ni_{1-x}Mg_xAl_2O_4$ spinels (Liu et al., 2014; Torrente-Murciano, 2016), increasing the available MSA.

Fig. 1(a and c) show bright-field STEM micrographs and Ni particle size distribution of the $Ni_{0.2}$ and $Ni_{0.4}$ catalysts reduced at 600 °C. $Ni_{0.2}$ and $Ni_{0.4}$ exhibit narrow Ni particle size distributions, and the average particle size increases from 8.7 nm for $Ni_{0.2}$ to 10.6 nm for $Ni_{0.4}$. Besides, HRTEM images of the reduced $Ni_{0.2}$ and $Ni_{0.4}$ catalysts are also reported in Fig. 1(b and d), and lattice fringes of d = 0.2079 nm for $Ni_{0.2}$ and d = 0.2081 nm for $Ni_{0.4}$ are obtained, consistent with the (111) crystal plane of Ni. The observed lattice fringe values indicate no significant difference in the interplanar distances of Ni after increasing Ni-Fe contents. Consistently with XRD data, no segregated Fe crystalline phase forms upon reduction. However, it should be noted that the statistical analysis of the particle size distribution focused on the larger metallic particles offering a clear contrast in the bright-field STEM images. Smaller metal clusters were not visualised by microscopy and normally remain undetected with XRD. Thus, their presence cannot be ruled out.

Moreover, high angle annular dark field (HAADF)-EDX mapping results for the $Ni_{0.2}$ and $Ni_{0.4}$ catalysts reduced at 600 °C are also presented in Fig. S8. Elemental mapping shows the spatial distribution of Ni and Fe within individual particles, indicating the formation of alloy structure as proven in our previous study (C. Mebrahtu et al., 2018b). However, Fe is preferentially distributed on Ni particles (Fig. S8a) on the $Ni_{0.2}$ catalyst, while it is also present over the support in small amounts on the $Ni_{0.4}$ catalyst (Fig. S8b).

Thus, the presence of i) small Ni-Fe particles, ii) the increased MSA/metal dispersion, and iii) increased reduction degree after the reduction treatment at 600 °C in H_2 with the increased Ni loading ($Ni_{0.12}$ - $Ni_{0.6}$) are related to the partial coverage of Ni particles from the support and strong metal-support interaction at low Ni loadings. The latter phenomenon is reasonable, considering the principles of the coprecipitation method during the catalyst synthesis. At the same time, the homogenous distribution of Mg (Fig. S8a and S8b) suggests the presence of vicinal metallic and basic sites available for catalysis. In addition, the less homogenous distribution of Fe on the $Ni_{0.4}$ catalyst shown by EDX mapping, compared with the $Ni_{0.2}$, indicates a variation of the local Fe/Ni ratio on the particles with different Ni loadings.

3.2. *Activity, selectivity, and stability of the hydrotalcite-derived catalysts for CO_2 methanation*

The activity of the catalysts in the CO_2 methanation reaction was tested at 300 °C and 1 atm in a fixed bed reactor under

Table 2 – Metallic surface area, as determined by CO Chemisorption analysis after reduction in H_2 at 600 °C for 2 h with a rate of 10 °C/min.

#	Catalyst	Metallic Surface Area (m^2/g_{cat})	M[a] (-)	Dispersion (%)	Reduction Degree (%)[b]
2	$Ni_{0.12}$	0.71	0.059	0.55	78
3	$Ni_{0.2}$	2.52	0.210	1.53	87
4	$Ni_{0.4}$	9.31	0.767	3.15	90
5	$Ni_{0.6}$	12.08	1.000	3.23	90
6	$Ni_{0.75}$	4.13	0.347	0.96	92

[a] M is the relative metallic surface area, dimensionless, = $\frac{MSA_{Cat}}{MSA_{Ni_{0.6}}}$, see Section 2.2 for details.

[b] Reduction degree of the catalysts based on H_2-TPR measured after reduction of the samples in H_2 at 600 °C, using the same reduction procedure employed before the catalytic testing.

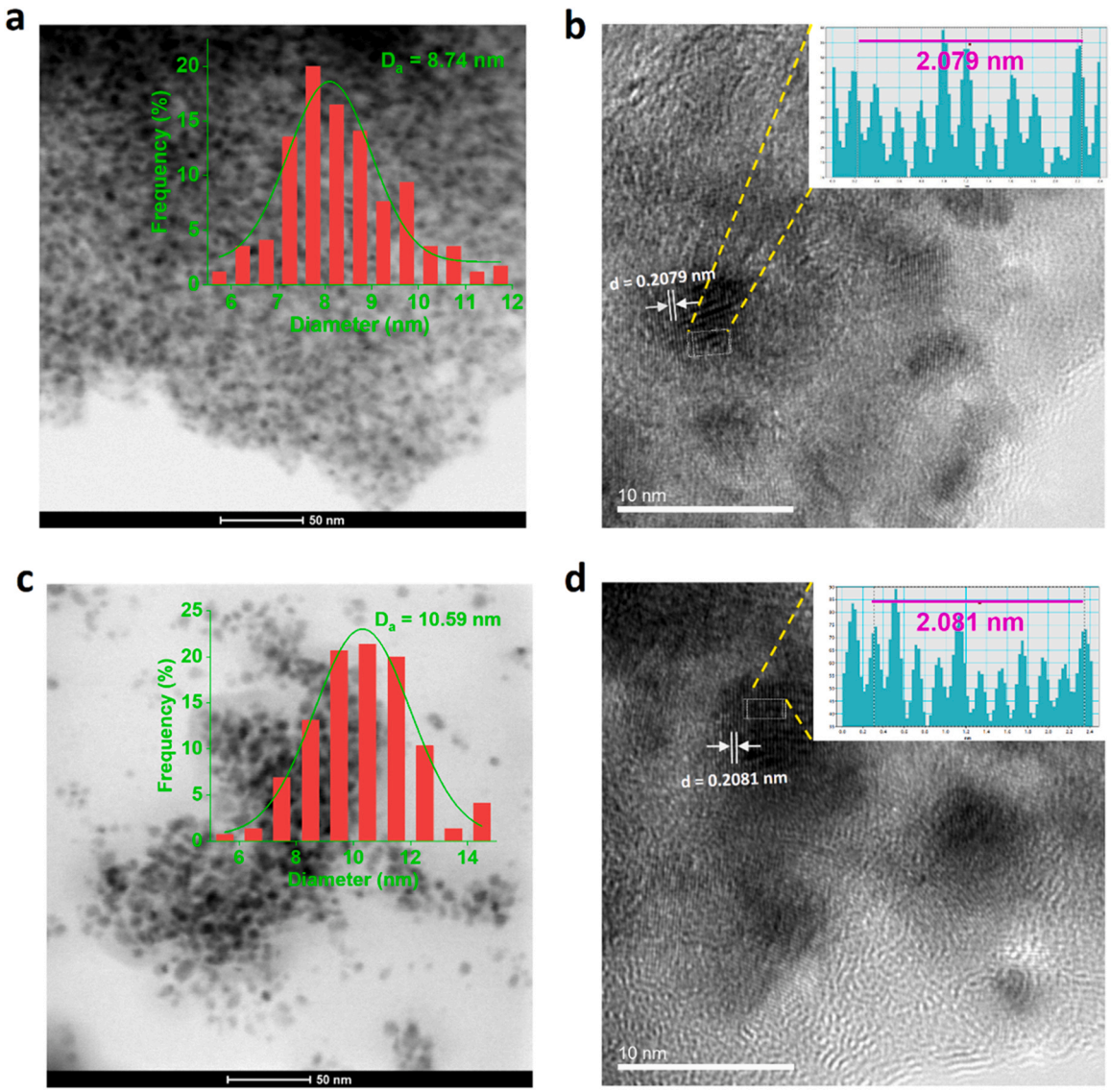

Fig. 1 – Bright-field STEM and HRTEM images of $Ni_{0.2}$ (a and b) and $Ni_{0.4}$ (c and d) catalysts after reduction at 600 °C under H_2, particle size distribution from larger area maps are included in a and c, and line scan profiles of the linear features in the HRTEM images are shown on top-right sides of b and d.

high space velocities to simulate those relevant for industrial use. No other products except CH_4 and CO were detected under the investigated conditions. The temperature of 300 °C, lower than most of those investigated in the literature (typically > 400–450 °C), is to evaluate the catalytic behaviour under conditions relevant to industrial use. At higher reaction temperatures, the conversion of CO_2 becomes limited from the thermodynamic equilibriums and thus the full conversion necessary for industrial use cannot be achieved. At the same time, we noted that the results obtained at higher reaction temperatures are not representative of the nature of the active sites and their stability at these lower reaction temperatures (Mebrahtu et al., 2019). To obtain a more precise estimation of the activity at 300 °C, the behaviour in a temperature range around this value was determined, and then deriving the precise value for reference 300 °C, as described in the experimental part. Testing operations were selected to avoid mass- and heat-transfer limitations, indications also supported by conventional experimental and calculation tests.

The Ni_0 shows no activity due to the absence of nickel and iron. The rate of CO_2 conversion per gram of catalyst ($r^m_{CO_2}$, Fig. 2a) increases with the Ni loading up to the $Ni_{0.4}$ catalyst ($r^m_{CO_2} = 0.37 mmol{\cdot}s^{-1}{\cdot}g^{-1}_{cat}$) and decreases at high Ni loading. Note that $Ni_{0.6}$, as compared to $Ni_{0.4}$, shows the largest MSA but a lower $r^m_{CO_2}$. A similar trend was also shown by the methane production rate per mass of catalyst ($r^m_{CH_4}$) which is maximised in the case of $Ni_{0.4}$ and $Ni_{0.6}$ ($r^m_{CH_4} \approx 0.29 mmol{\cdot}s^{-1}{\cdot}g^{-1}_{cat}$). $Ni_{0.12}$ and $Ni_{0.2}$ show comparatively lower $r^m_{CO_2}$ and $r^m_{CH_4}$ and larger production rates of CO per mass of catalyst (r^m_{CO}) due to the reverse water gas shift reaction.

We note that r^m_{CO} decreases with the Ni loading. The increased selectivity to CH_4 with increasing Ni loading (Fig. 2b) confirms this trend. In contrast, the rate data normalised by the Ni and Fe in moles ($r^n_{CO_2}$) highlight that the performance of $Ni_{0.2}$ is very similar to $Ni_{0.12}$ and $Ni_{0.4}$ (Fig. S9). Note that the apparent low selectivity to methane is due to the low conversion (< 10–15%) in these tests. The catalysts at higher CO_2 conversion show over 98–99% selectivity to methane.

The $Ni_{0.4}$, $Ni_{0.6}$ and $Ni_{0.75}$ catalysts show a stable behaviour for over 60 h of time on stream (TOS), whereas $Ni_{0.12}$ and $Ni_{0.2}$ deactivate during the 60 h catalytic tests (Fig. 2c, stability trend for $Ni_{0.2}$). The CH_4 selectivity remains stable

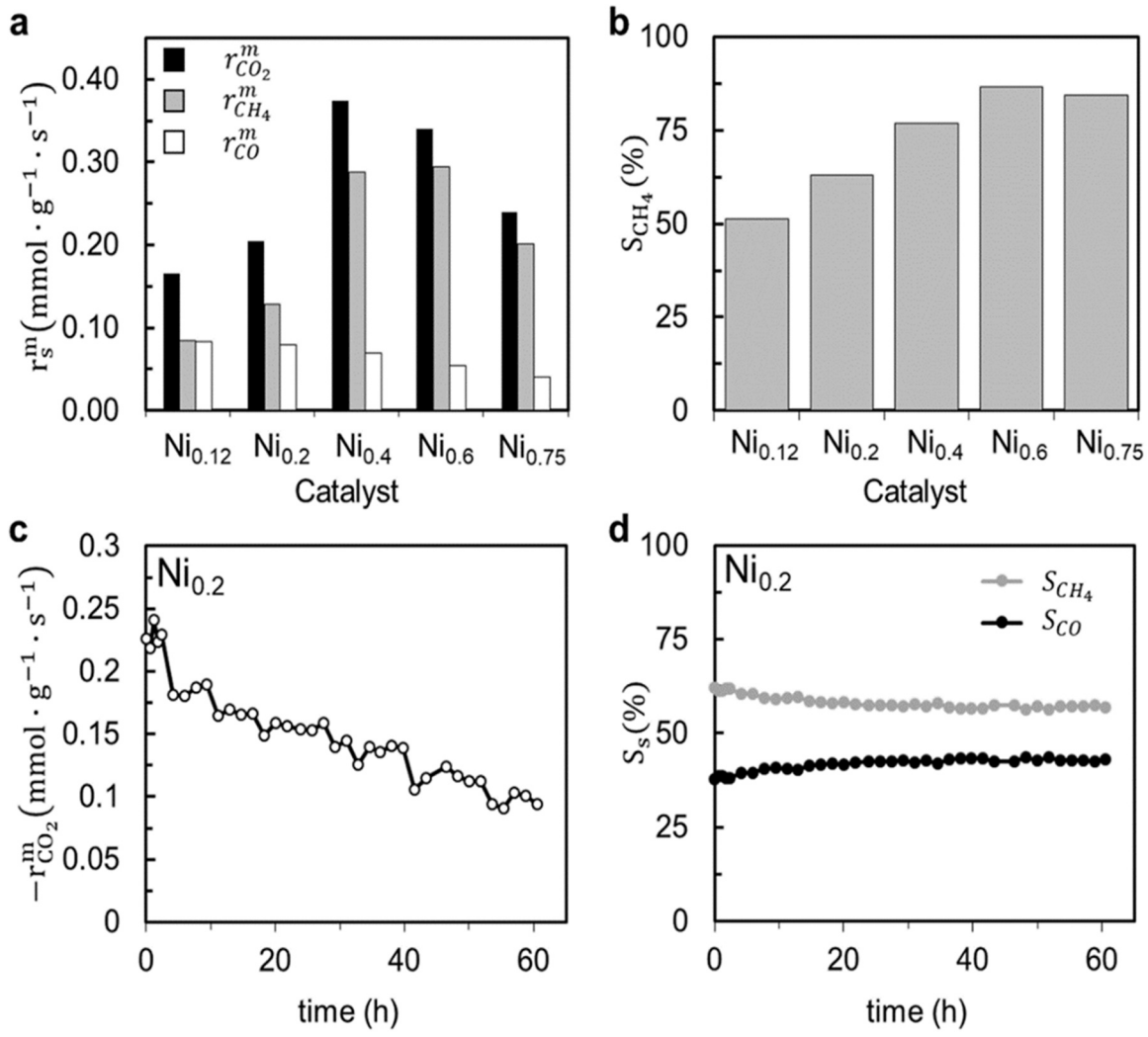

Fig. 2 – (a) CO_2 conversion, CO and CH_4 production rates normalised by the mass of the catalyst, obtained under differential reaction conditions (Eqs. 5 – 7); (b) CH_4 Selectivity of all prepared catalysts; (c) stability, and (d) selectivity of $Ni_{0.2}$ during 60 h (300 °C, P = 1 atm, H_2:CO_2 = 4:1, GHSV = 66,845 h^{-1}); in Figure (b) $S_{CO}(\%) = 100 - S_{CH_4}(\%)$.

after an initial decrease from 61% to about 57% (Fig. 2d), while the opposite trend was observed for CO selectivity. However, a stable behaviour could be observed (Fig. S10) if the $Ni_{0.2}$ catalyst is prereduced in H_2 at a higher temperature (900 °C). In these reduction conditions, the sintering leads to partial exsolution of Ni with the creation of small Ni crystallites. This evidence indicates that the deactivation is associated with Ni in the spinel structure, while the formation of Ni-supported crystallites leads to stable operations. Further indications will be given later in the section related to *in-situ* APXPS, NEXAFS, and DRIFTS studies.

Table S3 also summarises a comparison of TOF_{CO_2} values of the best catalysts obtained herein ($Ni_{0.4}$ and $Ni_{0.6}$) with both promoted hydrotalcite-derived and other catalysts reported in the literature. As shown in Table S3, Cu, La, V, Mn promoted NiMgAl hydrotalcite derived catalysts (Summa et al., 2022, 2021; Wierzbicki et al., 2018; Xiao et al., 2021) and Ce, V, Fe promoted Ni/Al_2O_3 catalysts (Daroughegi et al., 2021; Garbarino et al., 2021; Mebrahtu et al., 2018a) investigated by other groups show significantly lower TOF_{CO_2} values (at comparable low reaction temperature operations) than those reported here for the best samples. In addition, these samples were also tested under much higher space velocities. By comparing the results of TOF_{CO_2} with those of industrial catalysts (Abate et al., 2016; Mebrahtu et al., 2018b, 2019), it may be concluded that $Ni_{0.4}$ and $Ni_{0.6}$ samples outperform the behaviour of industrial catalysts for CO_2 methanation. They are thus representative samples for the *in-situ* studies.

3.3. *APXPS and NEXAFS studies, dependence on the reacting atmosphere*

After the proper selection of representative samples discussed in the previous section, the core of this study regards the *in-situ* mechanistic studies by a combination of physicochemical methods. Earlier studies by us (Giorgianni et al., 2020) analysed only the role of iron in hydrotalcite-based Ni-Fe catalysts for CO_2 methanation. Reported here is instead an analysis of the role of the fractional density of basic to metallic sites and the dependence on the reacting atmosphere. As commented before, literature studies focused on *ex-situ* correlations. We report here both *ex-situ* and *in-situ* data and the latter's dependence on the reacting atmosphere for a more comprehensive analysis of the reaction mechanism.

The $Ni_{0.2}$, $Ni_{0.4}$, and $Ni_{0.6}$ catalysts were studied by *in-situ* APXPS (ambient pressure X-ray photoelectron spectroscopy) and NEXAFS (X-ray absorption near edge structure) to clarify the Ni, Fe, and C speciation and how these change under the

reactive atmosphere (sequence of experiments and measured spectra were summarised in Table S4).

Fig. 3 shows the Ni electronic structure of the *in-situ* measured catalysts. Fig. 3a – c reports the Ni L-edges NEXAFS spectra in electron yield, whereas the Ni2p XPS spectra are reported in Fig. 3d – f. The Ni L-edges NEXAFS spectra are characterised by resonances arising from the electronic transition from the ground state $2p^6 3d^8$ to excited state $2p^5 3d^9$, where the presence of a multiplet structure indicates that Ni is mostly oxidised in these conditions due to the low H_2 pressure (50 – 70 mbar) used during the *in-situ* reduction. The maximum of the Ni L_3-edge resonance for $Ni_{0.2}$ and $Ni_{0.4}$ at around 853.4 eV under H_2 atmosphere (Hy2) and the presence of a small resonance on the high energy side of the main L_3-edge resonance are consistent with multiplet effects in Ni(II) species; a contribution from covalent Ni(III) species is also possible (Giorgianni et al., 2020). The small satellite peak above the L_3 edge at around 858 eV is due to ligand-to-metal charge transfer, typical of solid compounds. The comparative analysis of the Ni L-edges NEXAFS spectra for the three samples under the H_2 atmosphere at 300 °C (Hy1, Hy2; a black curve in Fig. 3a – c) shows that the intensity of the main resonance decreases in the order $Ni_{0.6} < Ni_{0.4} < Ni_{0.2}$, whereas the edge jump follows an opposite correlation amongst the samples.

In the case of the $Ni_{0.6}$, the maximum of the main resonance is shifted to a lower energy value, and a multiplet structure in the L_2 edge is much less evident. This indicates that $Ni_{0.6}$ also contains metallic Ni. It is the most reduced among the studied samples, in agreement with H_2-TPR data (Fig. S5). For the other samples, indications on metallic Ni can be deduced by comparing the spectra under hydrogenation and methanation reaction conditions, with the latter showing a more intense main resonance and a more pronounced multiplet structure consistent with catalysts in a comparatively more oxidised state. Under methanation conditions (M1, M2), the electronic structure of Ni changes more significantly for $Ni_{0.6}$, as shown by the relatively more pronounced increase in the intensity of the main resonance.

The XPS Ni2p spectra provide additional information on the surface speciation under different conditions. Initially, we used a 4-component fitting model developed previously on similar catalytic systems (Arrigo et al., 2020; Giorgianni et al., 2020). The Ni2 component at 852.6 eV in the $2p_{3/2}$ core level spectrum, found with an additional satellite peak at 5.7 eV above the mainline, is due to metallic Ni. Ni3 component at 853.7 eV is attributed to Ni(II) in NiO. The Ni4 component at *ca.* 855.8 ± 0.05 eV, accompanied by two intense satellite peaks at 861.1 eV and 864 eV, is due to a mixed Ni(II)/Ni(III) oxy-hydroxide phase. The Ni5 component, found at 859.1 eV, is attributed to cationic Ni in mixed oxides such as Ni aluminate species. We first discuss the dynamics involved for $Ni_{0.6}$ (Fig. 3f).

Accordingly, in the H_2 atmosphere (Hy1), the freshly reduced catalyst is predominantly reduced, whereas, under

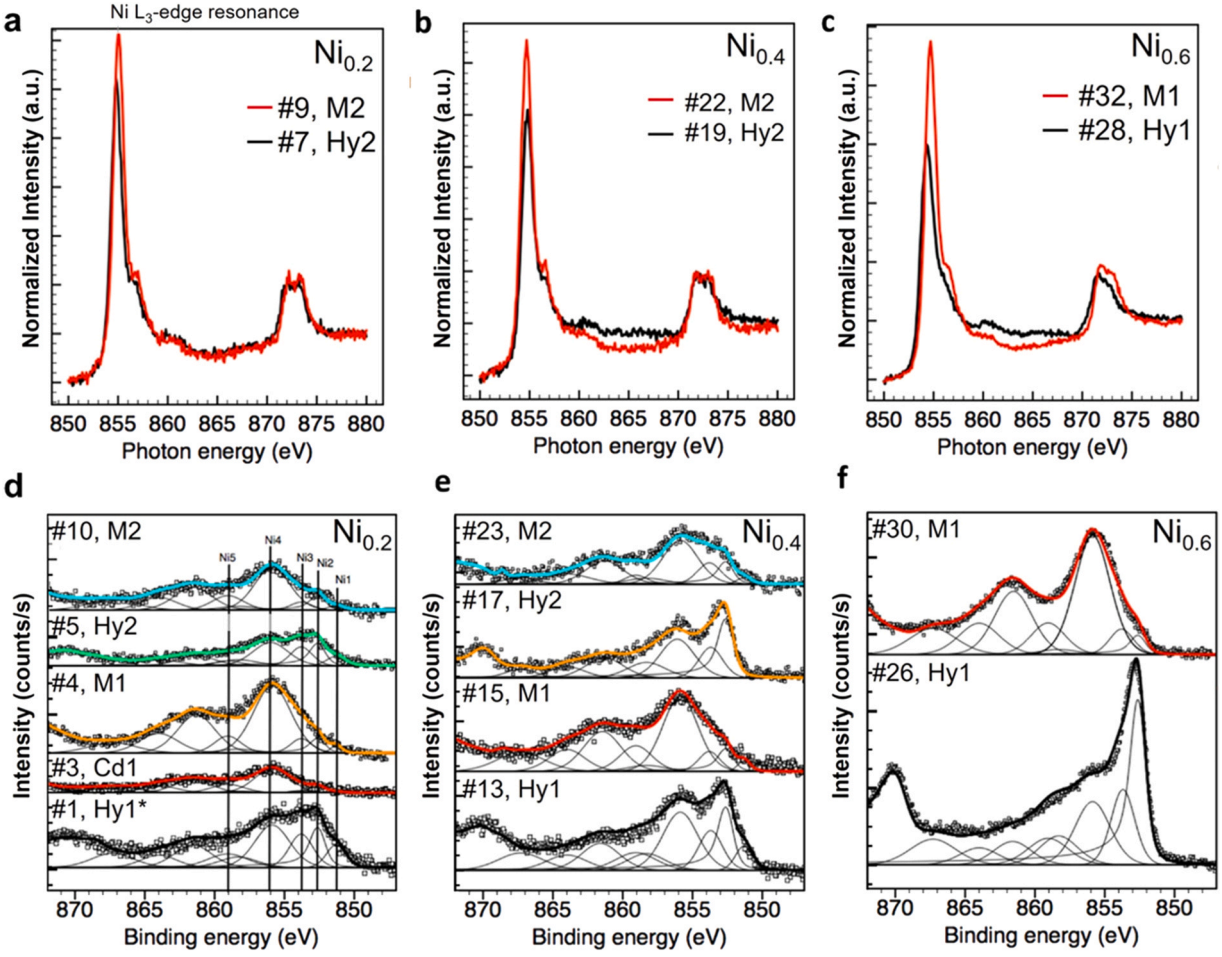

Fig. 3 – Comparison of the Ni electronic structure in H_2 (Hy1, Hy2: 4 mbar, 300 °C; Hy1 * 5 mbar, 600 °C), and methanation condition (M1, M2: H_2/CO_2 = 4, 5 mbar, 300 °C) by Ni L-edges NEXAFS (a – c), and Ni 2p XPS spectra (d – e) for the $Ni_{0.2}$, $Ni_{0.4}$ and $Ni_{0.6}$ catalysts. Before the measurements, the samples were reduced *in-situ*, at 600 °C in 50 – 70 mbar of H_2 (# represents the sequential number of the spectra; @ in Hy@, Cd@, M@ stands for the cycle number of the treatment; details in Table S3).

methanation reaction (M1), the surface becomes hydroxylated, as shown by the pronounced increase of the Ni4 component and the corresponding decrease of the Ni2 species. This result is consistent with previous work (Giorgianni et al., 2020) on high-Ni-content hydrotalcite-derived systems and describes the electronic structure dynamics of relatively large Ni nanoparticles. The fitting of the Ni 2p XPS spectra of $Ni_{0.4}$ and $Ni_{0.2}$ shows the presence of an additional low abundant component (Ni1) at lower BE (~ 851.4 eV). The latter component is visible in the H_2 environment, with a decreasing trend from Hy1 to Hy2, and nearly completely disappears under methanation conditions (M1 and M2). This species is relatively more abundant in the low-loaded $Ni_{0.2}$. Previously, a species at lower BE than the metallic Ni component was found for H-chemisorbed surface states (Denecke and Martensson, 2005) and single Ni atoms dispersed on a Cu single crystal (Koschel et al., 2000).

Such a shift to low BE indicates a photoemitting Ni metal atom, with a coordination number with the surrounding Ni atoms below the value of bulk metallic Ni (*fcc* is 12). From an electronic structure viewpoint, such a low BE species implies an accumulation of charge on the Ni atom if compared to the case of metallic Ni species with a full Ni-Ni coordination shell. Hence, using APXPS, we can identify the presence of metallic few-atom Ni clusters (Ni1 component), which occur at 851.4 eV BE. Under methanation conditions, we observe the transformation of the metallic Ni components into hydroxylated species.

However, the Ni2 component is relatively more abundant on $Ni_{0.4}$ if compared to $Ni_{0.6}$, consistent with the higher methane formation for the former. Moreover, the Ni1 components are still present on $Ni_{0.2}$ and $Ni_{0.4}$ under methanation reaction conditions instead of the complete oxidation observed under the CO_2 atmosphere (Fig. 3d). We also note that the metallic Ni2 component becomes relatively more intense for $Ni_{0.4}$ in the second reduction cycle (Hy2; H_2: 4 mbar, 300 °C; Fig. 3e). The formation of different Ni species after reduction is related to the reducibility of the catalysts and the effect of the instability of the sample towards sintering.

As shown in the H_2-TPR (Fig. S5), catalysts with lower Ni loading (such as $Ni_{0.2}$) require a higher reduction temperature compared to the catalysts with high Ni loading ($Ni_{0.6}$, for example). A catalyst that shows a high reduction temperature in the H_2-TPR ($Ni_{0.2}$) is characterised by a lower Ni2 component in Ni 2p XPS and *vice versa*. Moreover, the reduced $Ni_{0.2}$ catalyst also showed Ni1 species in addition to the bulk metallic Ni, while reduced $Ni_{0.6}$ did not show such species. We consider this a clear effect of the surrounding composition and the metal-support interaction. It will be shown later the implications on the surface C species.

The Fe L_3-edge NEXAFS spectra for the measured catalysts are reported in electron yield mode in Fig. 4. In this case, the Fe1 (708 eV), Fe2 (708.7 eV) and Fe3 (710.6 eV) components, assigned to Fe(0), Fe(II) and Fe(III) species, were found. The latter components changed dynamically in H_2 and methanation environment.

In the $Ni_{0.6}$, Fe is mostly metallic in the H_2 atmosphere, while, under methanation conditions, it gets oxidised into a Fe(II)/Fe(III) mixture. In comparison, under the H_2 atmosphere (Hy1 and Hy2), Fe in the $Ni_{0.2}$ and $Ni_{0.4}$ catalysts appear less metallic in character than $Ni_{0.6}$ (peak maximum still in correspondence of the Fe2 resonance). At the same time, under methanation conditions, their behaviour is consistent with the one shown by $Ni_{0.6}$.

In a previous study (Giorgianni et al., 2020), we showed that the condition in which Fe(II) species were still present in the near-surface region coincided with some metallic Ni and indicated that this was necessary for forming methane. In contrast, the total oxidation of Fe(II) to Fe(III) and hydroxylation of Ni coincided with the formation of carbon monoxide (Giorgianni et al., 2020). Thus, Fe species close to Ni hinder the latter's oxidation by acting as an oxygen scavenger.

As indicated in a previous paragraph, the most active samples are low Ni-loaded samples with an activity that increases in the following order $Ni_{0.2} < Ni_{0.6} < Ni_{0.4}$. The spectroscopic data so far indicate similar dynamics of the Fe and Ni species under methanation conditions for the three samples, with retention of a small amount of metallic Ni on the surface and a mainly quantitative oxidation/hydroxylation of Fe similar to previous work (Giorgianni et al., 2020). Although the transformations involved are of the same nature, we can identify in this work the existence of surface-exposed low nuclearity metallic Ni coordinated to metallic Fe atoms on the reduced samples.

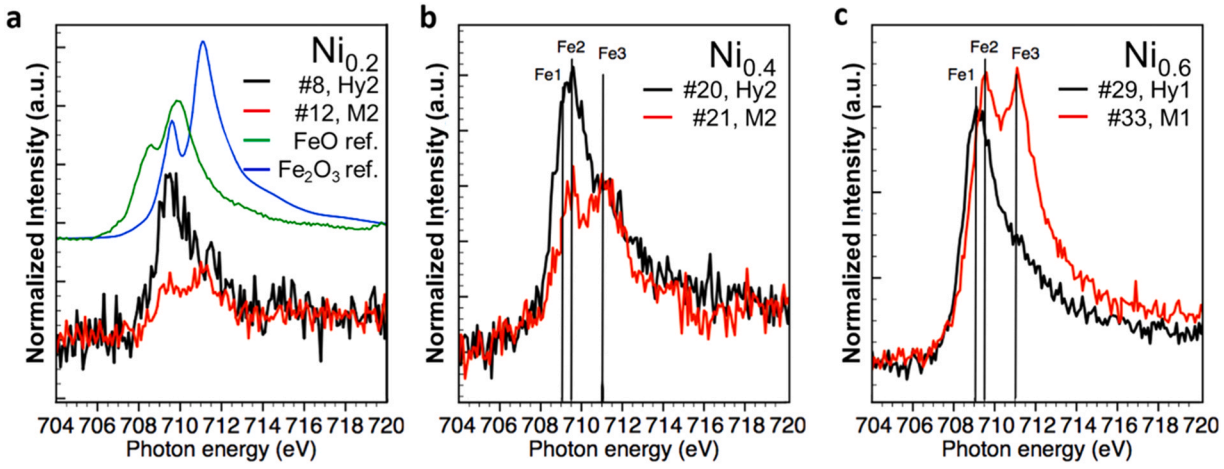

Fig. 4 – Comparison of the Fe electronic structure in H_2 (Hy1, Hy2: 4 mbar, 300 °C; Hy1 * 5 mbar, 600 °C), and methanation condition (M1, M2: H_2/CO_2 = 4, 5 mbar, 300 °C) by Fe L-edges NEXAFS for the $Ni_{0.2}$, $Ni_{0.4}$, and $Ni_{0.6}$ catalysts. Reference spectra for FeO and Fe_2O_3 are included in (a). Before the measurements, the catalysts were reduced *in-situ*, at 600 °C in 50 – 70 mbar of H_2 (# represents the sequential number of the spectra; @ in Hy@, Cd@, M@ stands for the cycle number of the treatment; details in Table S3).

This statement is correct because metallic Ni species are still present under methanation conditions in very small amounts commensurate with the amount of Fe (Ni/Fe ratio is 10). The mutual location of Ni and Fe atoms is such that the Ni-Ni coordination is below the bulk metallic Ni.

The C1s XPS spectra were fitted using a 7-component model (Fig. 5). The C1 component at 284.8 eV is associated with disordered sp^2 carbon with a high abundance of sp^3 moieties. It can also be due to small sp^2 domains within an amorphous carbon phase (Arrigo et al., 2022a). C-O bonds are found above 285.5 eV (Arrigo et al., 2022a). C2 at 286.3 eV was assigned to CO adsorbed linearly on metallic Ni surfaces (Wei et al., 2015) and methoxy species on oxides (Salmeron and Schlogl, 2008). The C3 component is at 287 eV, at which BE carbonic acid-like adsorbates derived from the interaction of CO_2 and H_2O were previously found (Ye et al., 2019). C4 and C5 are found at 288 eV and 288.5 eV, a region assigned to formate species, whereas the C6 component at 290 eV was assigned to carbonates (Salmeron and Schlogl, 2008). Above 291 eV, gas-phase CO_2 is found.

After the initial *in-situ* reduction treatment (50 – 70 mbar H_2, 600 °C), in the H_2 environment (Hy1), the surface of all the catalysts is still covered by carbonaceous species coming from the preparation procedure or the exposure to the environment (black spectra). We also note that, for $Ni_{0.4}$, under reduction conditions at 300 °C (Hy2, spectrum #18, Fig. 5b), it is possible to reduce the oxygenated carbonaceous species formed during the 1st methanation cycle (M1), with mainly deposited defective sp^2 C left. In contrast, on the second reduction cycle (Hy2) (spectrum #6, Fig. 5a) of $Ni_{0.2}$, it was not possible to remove all the oxygenated species formed after the 1st methanation cycle (M1). An interesting observation is that while for $Ni_{0.6}$ under *in-situ* conditions for methanation reaction, only a few C-O/methoxy (C2) and formate (C4) species are present, the surface of the $Ni_{0.4}$ and $Ni_{0.2}$ is characterised by a large population of oxygenated C species, including carbonate species, indicating a large population of Lewis basic sites available for CO_2 chemisorption under methanation conditions. The formate species (C4) are similar for $Ni_{0.2}$ and $Ni_{0.4}$ and much less abundant for $Ni_{0.6}$.

We note that the distribution of oxygenated species formed on $Ni_{0.4}$ during the first methanation cycle (spectrum #16, Fig. 5b) is similar to that of oxygenated species formed on $Ni_{0.2}$ during the second methanation cycle (spectrum #11, in Fig. 5a). However, for $Ni_{0.4}$, the distribution of the latter species changes over time in the second methanation cycle (spectrum #24, Fig. 5b), indicating ongoing structural changes (spectra #24 and 25, Fig. 5b). We also note that now hydrogenated/reduced C2 species are relatively more abundant on the $Ni_{0.4}$ during the second methanation cycle and a possible interconversion of one form into another occurs. For example, it was possible to identify for $Ni_{0.4}$ the presence of weakly interacting carbonic acid-like adsorbates (C3 in spectrum #25, Fig. 5b), probably intermediate species for the formation of other oxygenated species (*e.g.*, C2 in spectrum #24, Fig. 5b) or C accumulation (C1) upon stronger interaction with the catalyst surface.

$Ni_{0.6}$ shows the highest C accumulation (most intense C1 component; spectrum #31, Fig. 5c). We consider the latter related to this sample's larger Ni particle size. The presence of oxygenated species is correlated to the highly dispersed Ni species in the Ni2p seen in XPS, whose electronic structure indicates a high electron density, which is available for CO_2 chemisorption. The speciation of surface-oxygenated compounds reflects the reducibility and stability of the catalysts against sintering. $Ni_{0.2}$ is the least reducible and shows a large abundance of highly oxidised carbon species. $Ni_{0.4}$ initially presents similar characteristics in terms of C speciation; however, these carbon species appear to be easily reduced under hydrogenation conditions.

3.4. *In-situ DRIFTS experiments*

The nature of CO_2 chemisorbed species under CO_2-only atmosphere and methanation conditions was studied by *in-situ* DRIFTS (CO_2-DRIFTS and M-DRIFTS, respectively). The $Ni_{0.2}$, $Ni_{0.4}$, and $Ni_{0.6}$ were measured at 200, 300, and 400 °C, together with a commercial Ni/Al_2O_3 catalyst methanation catalyst for comparison (CRG-F, from British Gas) prepared by a similar coprecipitation method. In this industrial sample, the Ni and Al molar fractional loadings, x_M^L, are 0.306 and 0.155, respectively. The composition is between $Ni_{0.2}$ and $Ni_{0.4}$; see Table S1. Steady-state CO_2- and methanation-DRIFTS spectra were recorded after exposing the catalyst to

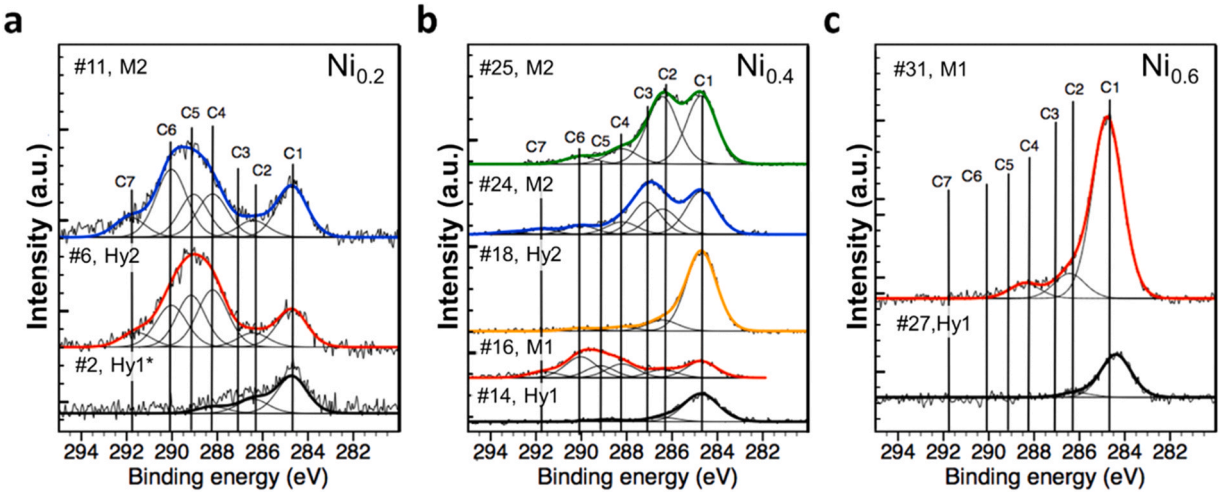

Fig. 5 – Fitted C1s spectra at KE 400 eV for $Ni_{0.2}$, $Ni_{0.4}$, and $Ni_{0.6}$ in H_2 (Hy1, Hy2: 4 mbar, 300 °C; Hy1 * 5 mbar, 600 °C), and methanation condition (M1, M2: H_2/CO_2 = 4, 5 mbar, 300 °C). Major and minor tick labels are consistent between the plots. Before the measurements, the catalysts were reduced *in-situ*, at 600 °C in 50 – 70 mbar of H_2 (# represents the sequential number of the spectra; @ in Hy@, Cd@, M@ stands for the cycle number of the treatment; details in Table S3).

the reaction environment for 10 and 30 min, respectively (Fig. 6). All the recorded spectra show the characteristic double band of CO_2 in the gas phase at 2359 and 2343 cm^{-1} (Coenen et al., 2018).

During CO_2-DRIFTS experiments (Fig. 6a), monodentate carbonate (1550, 1410 cm^{-1}), bidentate carbonate (1275–1330, 1625–1670 cm^{-1}), bicarbonate (1220, 1370–1405, 1655–1670 cm^{-1}), and formate species (1330–1400, 1600 and 2870 cm^{-1}) are observed for the $Ni_{0.2}$ and $Ni_{0.4}$ catalysts. Similar absorption bands were found on MgO (Busca and Lorenzelli, 1982). Conversely, the latter species are absent on the CRG-F and present only in traces on $Ni_{0.6}$ (Fig. 6a), probably due to the low MgO content in this sample. The band associated with adsorbed bicarbonate species (1220 cm^{-1}) remains very small within the whole temperature range investigated (200–400 °C) (Busca and Lorenzelli, 1982; Huynh et al., 2020). CO species adsorbed in the linear (2000–2130 cm^{-1}), bridge (1880–2000 cm^{-1}), threefold (1800–1880 cm^{-1}), and fourfold (1800–1730 cm^{-1}) modes (Papadopoulos, 2008) were found for $Ni_{0.2}$, $Ni_{0.4}$ and on the CRG-F catalysts. Moreover, on the CRG-F catalyst, adsorbed CO was the most abundant species, in agreement with Fujita et al. (1993).

During M-DRIFTS experiments at 200, 300, and 400 °C (Fig. 6b), bands associated with methane in the gas phase (3016, 1306 cm^{-1} (Pan et al., 2014b)) and adsorbed water (2700–3700 cm^{-1} on MgO (Foster et al., 2005) and 1650–1600 cm^{-1} (Hadjiivanov, 2014)), potentially overlapping with bands of water in the gas phase (4000–3370, 1930–1118 cm^{-1} (Hakkarainen et al., 2000)) were detected. Bicarbonate species (1220 cm^{-1}) were not identified even at 200 °C, while formate (1330–1400, 1600 and 2870 cm^{-1}) and adsorbed CO bands increased as compared with CO_2-DRIFTS experiments. After increasing the temperature of the M-DRIFTS experiment from 200 to 400 °C, all the observed bands decrease in intensity, while the methane bands, at 300 °C, go through a maximum. Finally, we note a more pronounced increase in the bands associated with CO_2 intermediates, similar to what was found by Huynh et al. (2020). The more intense bands associated with adsorbed water are found on the $Ni_{0.2}$ and $Ni_{0.4}$ catalysts at 200 °C.

The presence of multiple CO bands, evidenced by CO_2-DRIFTS experiments, indicates the presence of dissociative adsorption of CO_2 (Fig. 6a) on the surface of metallic Ni, in agreement with the literature (Heine et al., 2016; Völs et al., 2021; Yuan et al., 2016). At the same time, the presence of bicarbonate and formate species indicates the presence of an associative CO_2 adsorption mechanism due to MgO (Fujita et al., 1993; Ho et al., 2020; Huynh et al., 2020; Miao et al., 2016). The presence of CO, bicarbonate, and formate species

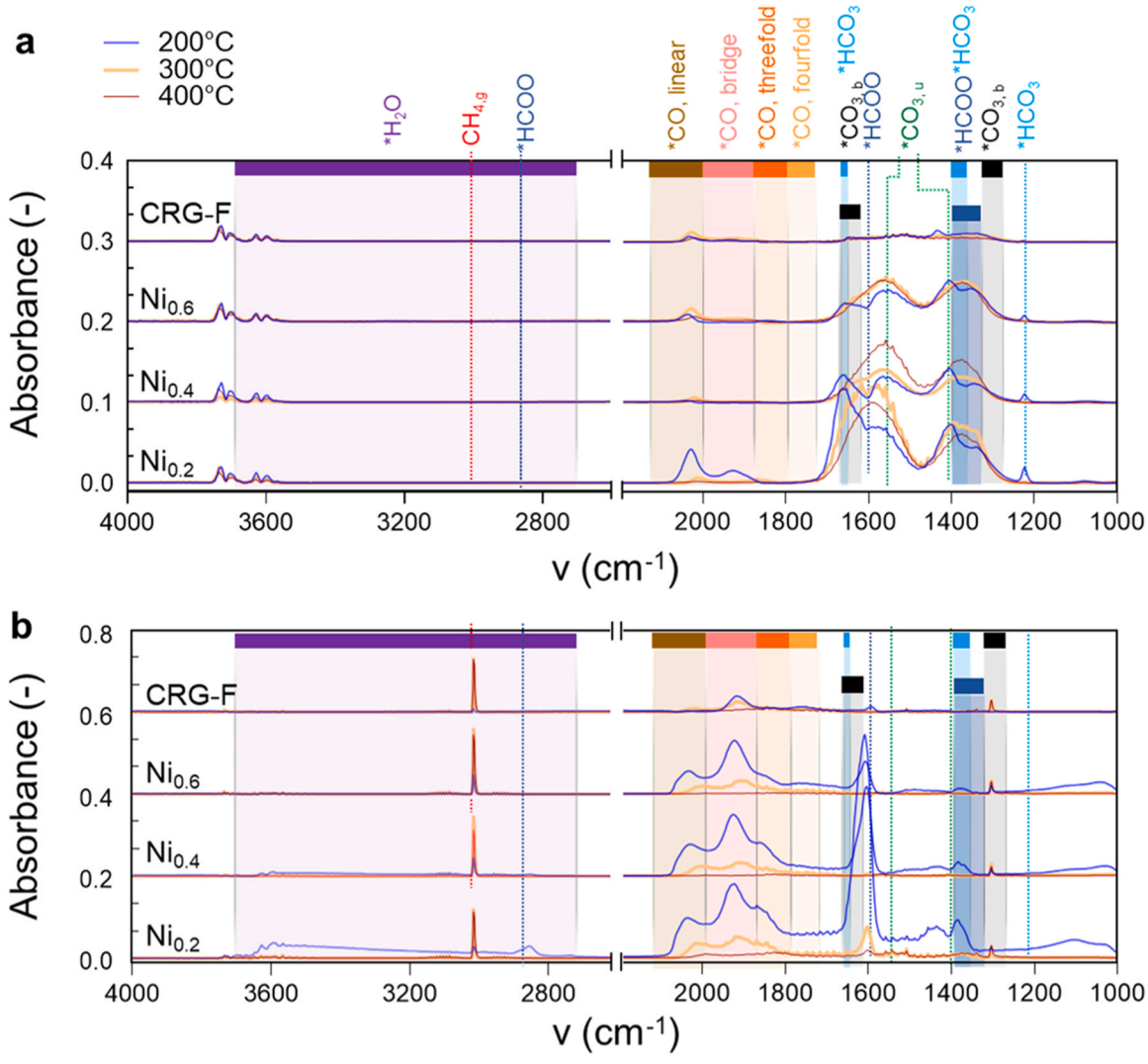

Fig. 6 – *In-situ* DRIFTS spectra recorded during (a) CO_2 adsorption (feed 50 mL/min, CO_2/N_2 = 1/9 v/v), and (b) Methanation experiments (Total feed = 50 mL/min, $CO_2/H_2/N_2$ = 1/4/1 v/v).

during the M-DRIFTS experiment is consistent with C1s APXPS results (Fig. 5).

4. Discussion

Before analysing the structure-activity relationships identified in this work, and the new insights into the state-of-the-art, it is useful to briefly recall the main indications from the study reported in the previous section.

A series of hydrotalcite-based Ni-Fe catalysts were synthesised to study these materials in the low-temperature (300 °C) CO_2 methanation for the motivation outlined before. In short, high activity at these reaction temperatures is needed from an industrial perspective because the maximum conversion is limited by equilibrium at higher temperatures. With respect to earlier literature mechanistic studies, this is the first investigation made on methanation catalysts operating in this low-temperature range. On the other hand, we earlier note that the catalyst dynamic and effect of the reaction environment strongly depend on the reaction temperature (Giorgianni et al., 2020; Mebrahtu et al., 2019). From this perspective, this manuscript thus provides new insights because measurements were made under different conditions to literature and thus tailored to understand *in-situ* catalyst dynamics and mechanistic aspects at this industrially-relevant temperature of operation. In contrast, literature data are *ex-situ* or made for much higher temperature operations and less active catalysts.

For this reason, the catalysts were prepared to have a high activity at these low-temperature conditions. The catalysts were thus reduced at 600 °C rather than higher temperatures, because the sintering occurring above 600 °C would prevent obtaining such high activity. The catalytic tests confirm the high rate of CO_2 methanation of these catalysts and thus their suitability for mechanistic study. The best performances are shown by $Ni_{0.4}$ sample. Still, the *in-situ* study was extended to $Ni_{0.2}$ and $Ni_{0.6}$ samples to have a homogeneous series of samples where the Ni metallic area and density of basic surface sites change.

These three catalysts were studied by combining different *in-situ* spectroscopy techniques (APXPS, NEXAFS and DRIFTS), monitoring the change in the nature of the surface species as a function of the reactive environment. Parallel *ex-situ* studies (H_2-TPR, CO2-TPD, CO-chemisorption) combined with structural (XRD) and morphological analysis (SEM, HRTEM, and surface area/porosity measurements) provide the complementary data to compare these samples with literature for which typically only *ex-situ* measurements were reported.

Hydrotalcite-derived materials are more active and stable towards CO_2 methanation than other oxide-supported Ni-based catalysts (such as Ni/Al_2O_3), confirming the previous results (Hwang et al., 2012; Mebrahtu et al., 2018b). In contrast to earlier reports concluding that high active metal loading (75–80% of Ni) was needed for viable CO_2 conversion rate per gram of catalyst (Bette et al., 2016; Mebrahtu et al., 2018b; Silva et al., 2010), we show herein that high catalytic activity can be obtained even with lower Ni-Fe loadings, with an optimal performance attained for $Ni_{0.4}$ (Fig. 2a).

4.1. Structure-activity correlations

To develop a structure-activity correlation for the CO_2 methanation, we first analyse the dependence of turnover frequencies (TOFs) on the density of metallic and basic sites, which are considered the descriptors of the catalytic behaviour. The results are rationalised based on *in-situ* DRIFTS, APXPS, and NEXAFS results and the distribution of basic and metallic active sites. Accordingly, the TOFs of CO_2 conversion (TOF_{CO_2}), CO (TOF_{CO}) and methane production (TOF_{CH_4}) are inversely correlated with the density of metallic sites (M) and metallic dispersions (measured by CO chemisorption, Fig. S11) and directly correlated with the total density of the basic sites ($B_{A,\ Total}$, CO_2-TPD). Due to the intercorrelation of basic and metallic sites on the prepared catalysts, the surface fraction of basic sites (X_B, defined in Section 2.2) is a better descriptor to evaluate the catalytic performance. We find that the measured TOF_{CO_2}, TOF_{CO}, and TOF_{CH_4} are exponentially correlated with the surface fraction of basic sites (X_B, Fig. 7). Similar correlations were found for basic or cerium sites (Liu et al., 2020).

Consistently with the C1s APXPS and DRIFTS results (Fig. 5a - b; Fig. 6), besides CO species, also high surface concentrations of bicarbonates and formate species are observed in the presence of large amounts of basic sites due to the improved CO_2 adsorption ability promoted by MgO (*i.e.* high X_B and low Ni loadings). CO is formed by the dissociative chemisorption of CO_2, while bicarbonates and formate *via* its associative chemisorption. Therefore, the increased TOF_{CO_2}, TOF_{CO},and TOF_{CH_4} over the $Ni_{0.12}$ and $Ni_{0.2}$ catalysts compared to $Ni_{0.4}$ and $Ni_{0.6}$ catalysts can be explained by assuming that the conversion of CO_2 into methane occurs through two simultaneous routes, namely the CO and formate routes (Scheme 1) in agreement with previous studies (Ho et al., 2020; Huynh et al., 2020; Miao et al., 2016; Millet et al., 2019; Pan et al., 2014a; Papadopoulos, 2008), but performed at higher reaction temperatures.

Accordingly, for catalysts with large X_B values, such as $Ni_{0.12}$ and $Ni_{0.2}$, the increased TOF_{CO_2}can be related to the high Mg loadings promoting CO_2 adsorption, while the large TOF_{CO} and TOF_{CH_4} can be related mostly to the increased surface concentration of CO and formate, in agreement with M-DRIFTS and APXPS. Specifically, the formation of CO, at low CO_2 conversion, during the methanation reaction is produced by the RWGS, and it is a key intermediate for the former reaction (Ko et al., 2016). According to the literature, the contribution by RWGS over Ni-based catalysts becomes significant under conditions such as i) short contact time or low Ni loadings/MSAs due to the lack of H-chemisorbed metallic sites for converting CO to CH_4 (Mathew et al., 2021), ii) imbalance between metallic Ni and Mg sites when formate decompose in the presence of Mg ion (Mathew et al., 2021), and iii) high Fe/Ni ratio in the presence of oxidised Ni due to the higher activity of Fe than Ni in promoting CO_2 dissociation (Ko et al., 2016; Mebrahtu et al., 2018b).

Instead, we observe in this manuscript that the most important factors enhancing RWGS reaction for these low-temperature methanation catalysts are the low MSAs at low Ni loading (due to partial coverage of Ni particles by the support (Xu et al., 2017)) and the large density of basic sites promoting the formate route. However, a locally high Fe/Ni ratio due to Ni-Fe alloys facilitates the RWGS reaction. Various synergistic factors induce the decreased CH_4 selectivity, favouring CO selectivity, at low Ni loadings. In the case of the $Ni_{0.4}$ and $Ni_{0.6}$ catalysts, as previously discussed, the low surface concentration of formate measured by M-DRIFTS (Fig. 6b) and *in-situ* APXPS (Fig. 5c) suggests a fast conversion of formate and CO into methane due to the high MSAs (Table 2).

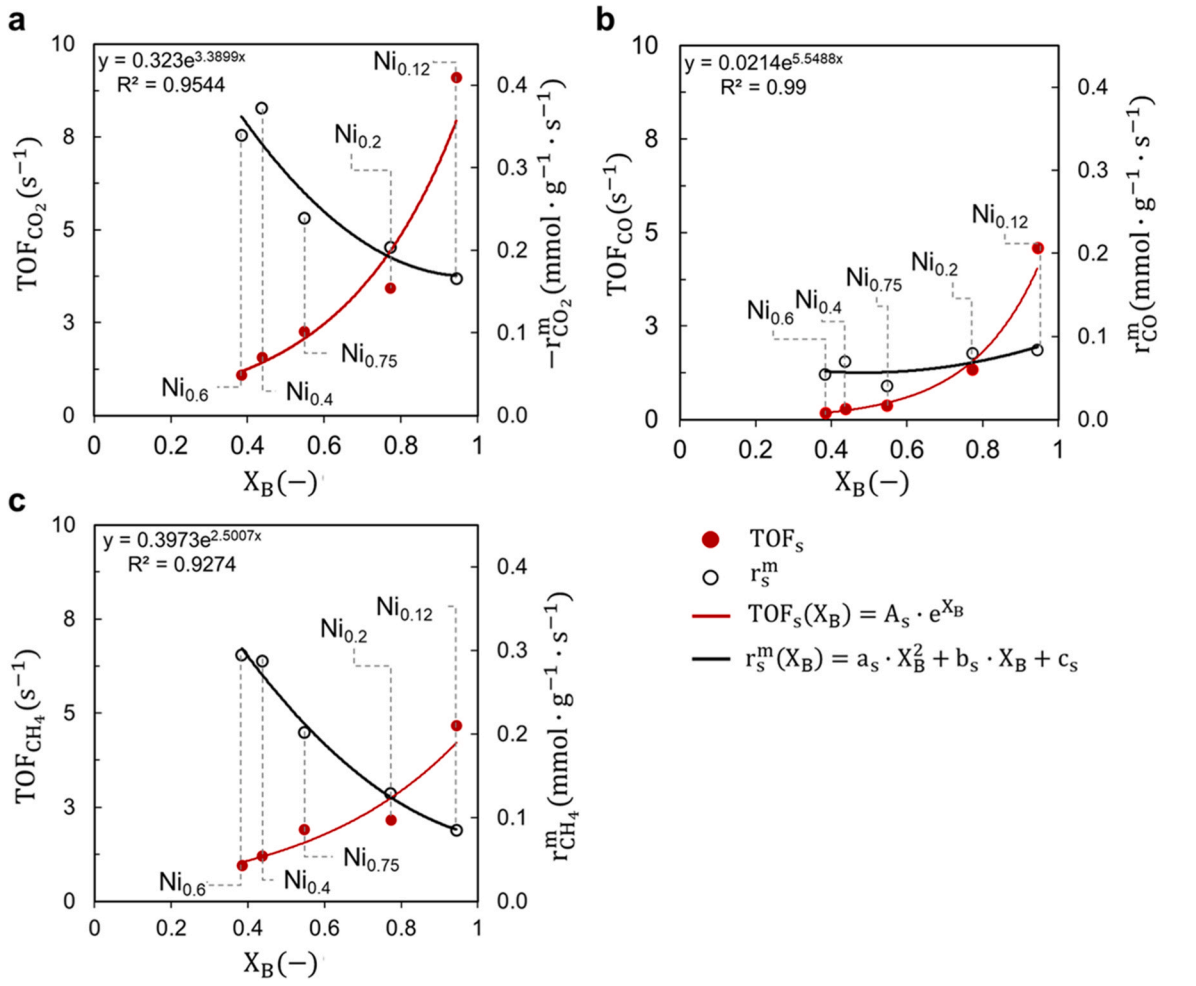

Fig. 7 – Relationship between CO_2, CH_4 and CO TOFs and rates of the measured catalysts with the fractional coverage of the basic sites (X_B and TOF_s defined in Eqs. 4 and 9, respectively; 300 °C, 1 atm, H_2:CO_2 = 4:1, 66,845 h^{-1}, under differential conditions).

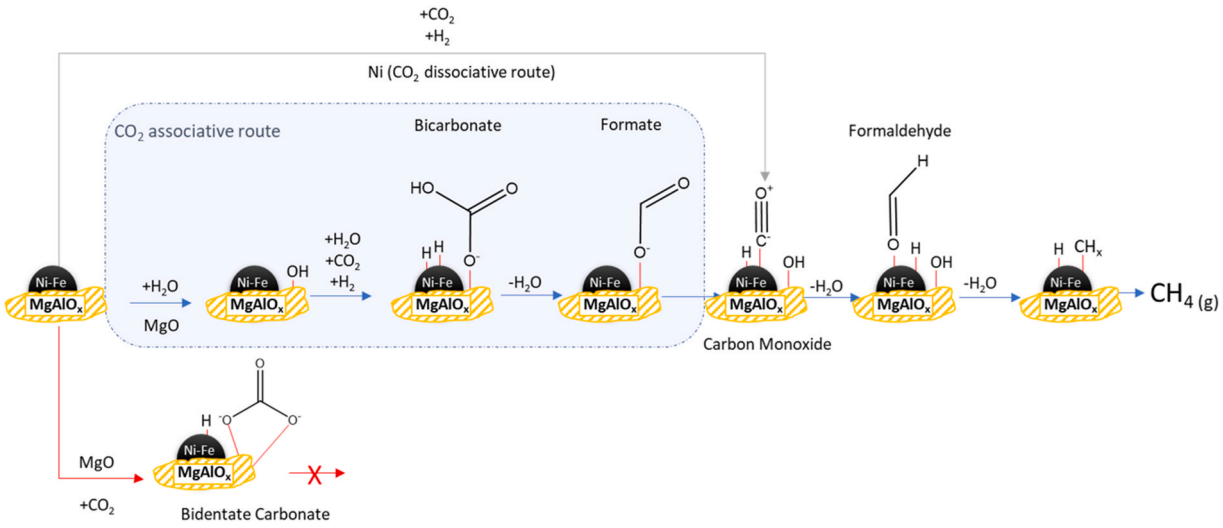

Scheme 1 – Proposed reaction mechanism of CO_2 methanation over Ni-Fe(Mg, Al)O_x catalyst.

Although the $Ni_{0.75}$ catalyst (*i.e.* prepared in the absence of Mg) showed TOFs in between the $Ni_{0.2}$ and $Ni_{0.4}$ (Fig. 7) and superior to the $Ni_{0.4}$ and $Ni_{0.6}$ catalysts, its intermediate activity cannot simply be related to its intermediate X_B. The surface H availability is also important.

The lower TOF_{CO_2}, TOF_{CO}, and TOF_{CH_4} for $Ni_{0.4}$ and $Ni_{0.6}$ might indicate that the limiting factor is not the formate and CO conversion to methane but rather the availability of sites for CO_2 adsorption, consistently with the measured high $r^m_{CO_2}$, $r^m_{CH_4}$, and low r^m_{CO} (Fig. 7). Instead, the conversion of formate and CO can be rate-limiting in the case of $Ni_{0.12}$ and $Ni_{0.2}$ (high X_B, low Ni MSA), *e.g.*, due to the low availability of metallic sites, in agreement with the low $r^m_{CO_2}$, $r^m_{CH_4}$, and the high r^m_{CO} (Fig. 7). The lower r^m_{CO} obtained over $Ni_{0.75}$, prepared

in the absence of Mg, is attributed to the negligible contribution from the formate route due to the lower total density of basic sites ($B_{Total, A}$, Table S2, Fig. S6).

4.2. *Changes during catalytic operations*

Deactivation of the $Ni_{0.2}$ catalyst during 60 h TOS (Fig. 2c) can be attributed to the oxidation of small Ni clusters. This oxidation of smaller Ni clusters is consistent with the large surface water concentration, as well as the fast oxidation of the Ni clusters that are formed upon pre-reduction of $Ni_{0.2}$ and are oxidised after introducing CO_2, as measured by M-DRIFTS (Fig. 6b) and, Ni2p XPS in methanation conditions (Ni1 component Fig. 3d), respectively.

The oxidation of Ni by decomposing CO_2 to CO is known (Heine et al., 2016; Völs et al., 2021; Yuan et al., 2016). Besides suppressing the methanation rate by competitive adsorption with CO_2 (Borgschulte et al., 2013; Marocco et al., 2018), strongly adsorbed water can oxidise small Ni clusters (Mebrahtu et al., 2019). In our previous work (Giorgianni et al., 2020), we attributed the deactivation of hydrotalcite-derived Ni-based catalysts to a water-mediated oxidative mechanism leading to hydroxylation of the Ni, which was less severe in the presence of Fe. On the contrary, the stability of the $Ni_{0.2}$ catalyst after reduction at 900 °C (Fig. S10) can be related to the absence of the small Ni clusters due to the higher temperature of reduction, causing the sintering of the smaller Ni clusters and thus a lower intrinsic activity. This clearly demonstrates how the use of catalysts active at a higher temperature range does not provide reliable information on catalysts active at lower temperatures.

4.3. *Mechanistic insights*

This work has provided new mechanistic insights into the complex dependence of the observed reaction rates on the structural characteristic of the catalysts. Concerning literature, these insights are related to a highly-active CO_2 methanation catalyst operating at 300 °C, as would be necessary for industrial operations, but having a Ni content below 50% wt. The structure-activity relationships discussed in Section 4.1 are, thus, related to this type of catalyst for the first time and obtained by both *ex-situ* and *in-situ* studies. Literature data refer to catalysts operating at higher temperatures with lower activity.

We identify for the first time highly dispersed metallic Ni-Fe clusters on $Ni_{0.2}$ and $Ni_{0.4}$. Due to their electronic structure, these species are expected to be highly reactive toward CO_2 chemisorption. However, deactivation due to excessive hydroxylation of the surface by water and consequent blockage of the sites for H chemisorption is an issue. Although Fe can mitigate this problem (Giorgianni et al., 2020), herein we show that the particle size, metal loading, and chemical composition in terms of Fe, Ni, and Mg surface distribution play an important role.

For $Ni_{0.2}$, the surface Fe is mostly distributed on Ni particles such that, as shown by APXPS, Fe-Ni ensembles are formed. However, an excessive hydroxylation is seen, possibly due to the high Mg loading. In contrast, we do not observe such Fe-Ni ensembles in $Ni_{0.6}$, possibly because of the low intermixing between Fe and Ni at high Ni loadings and low concentration of Mg during the synthesis in agreement with HAADF-EDX mapping data of $Ni_{0.4}$ (Fig. S8b).

The ideal situation is realised for $Ni_{0.4}$, in which not only the Fe-Ni clusters are still visible, with both Fe and Ni able to reduce CO_2 to CO *via* the direct route or *via* the formate route, but the abundance of metallic Ni is relatively high, which guarantees adjacent H-chemisorption sites for the further reduction of CO to methane.

This study exemplifies a catalyst design strategy to control product distribution under conditions for methanation reaction, in which a complex network of reaction pathways occurs. We show the important role of Mg, the Ni-Fe particles, and the intimate atomic distribution during the synthesis step. However, highly dispersed Mg close to the metallic particles can also assist in the formate route. This fact explains the apparent correlation of the activity with the density of basic sites, which is dominated by the adsorption of CO_2 on Mg sites and less on Ni-Fe sites. Hence, optimisation of the Mg and Ni contents allows particles with the optimal chemical composition for the methanation reaction.

5. Conclusions

In this work, a series of Ni-Fe hydrotalcite-derived catalysts with a wide range of Ni and Mg loadings were prepared by a coprecipitation method and employed for CO_2 methanation. Industrially relevant catalytic performance was obtained using the $Ni_{0.4}$ catalyst with a significantly reduced Ni loading compared to other commercial catalysts. Using the $Ni_{0.4}$ catalyst with intermediate Ni and Mg loadings, a CO_2 conversion rate of 0.37 mmol/g_{cat}/s is obtained at 300 °C. Note that selectivity to methane is affected by very high space-velocities and thus low CO_2 conversion in these tests to avoid mass- and heat-transfer limitations. At higher conversion, selectivity to methane is up to over 99% (Mebrahtu et al., 2018b, 2019). However, this aspect was not reported here because it is not relevant to the aim of the study: obtaining new mechanistic insights by combining *ex-situ* and *in-situ* data on a highly-active catalyst for CO_2 methanation at 300 °C having reduced Ni loading (< 50% wt) with respect to industrial catalysts for this reaction.

Its superior activity is attributed to the optimal distribution of basic and metallic sites, leading to dissociative CO_2 and Mg-assisted associative CO_2 chemisorption with forming formate species as intermediate. The intermediate density of metallic and basic sites is the key parameter to obtaining highly active and CH_4 selective catalysts during CO_2 methanation. We have identified structure-activity relationships in CO_2 methanation on these catalysts, which allow us to rationally tailor the stability and distribution of basic and metallic sites of hydrotalcite-derived catalysts.

Concerning the abundant literature on this topic, we have to remark that it refers to only less active and active catalysts at higher reaction temperatures or for which a full set of *ex-situ* and *in-situ* data supporting mechanistic insights is not available. Therefore, this paper provides a rationale for designing industrially competitive CO_2 methanation catalysts with high catalytic activity while maintaining low Ni loading for the first time.

Declaration of Competing Interest

The authors declare that they have no known competing financial interests or personal relationships that could have appeared to influence the work reported in this paper.

Acknowledgements

The authors want to acknowledge Diamond Light Source for beamtime allocation under proposal SI22687. This work was performed as part of the Cluster of Excellence Fuel Science Center (EXC 2186, ID: 390919832) funded by the Excellence Initiative by the German federal and state governments to promote science and research at German universities.

Supporting information

X-ray diffractograms of dried, calcined, and reduced samples with a detailed discussion, SEM micrographs of dried and calcined samples, a summary of textural properties and elemental compositions, H_2-TPR data, CO_2-TPD data, CO chemisorption data, HAADF-EDX mapping results, catalytic performances at different conditions, catalytic performance comparison with published results, *in-situ* APXPS and NEXAFS experimental details and structure-activity correlations.

Appendix A. Supporting information

Supplementary data associated with this article can be found in the online version at doi:10.1016/j.cherd.2023.03.026.

References

Abate, S., Barbera, K., Giglio, E., Deorsola, F., Bensaid, S., Perathoner, S., Pirone, R., Centi, G., 2016. Synthesis, characterization, and activity pattern of Ni–Al hydrotalcite catalysts in CO_2 methanation. Ind. Eng. Chem. Res. 55, 8299–8308. https://doi.org/10.1021/acs.iecr.6b01581

Abelló, S., Medina, F., Tichit, D., Pérez-Ramírez, J., Groen, J.C., Sueiras, J.E., Salagre, P., Cesteros, Y., Abello, S., Medina, F., Tichit, D., Perez-Ramirez, J., Groen, J.C., Sueiras, J.E., Salagre, P., Cesteros, Y., 2005. Aldol condensations over reconstructed Mg-Al hydrotalcites: structure-activity relationships related to the rehydration method. Chem. Eur. J. 11, 728–739. https://doi.org/10.1002/chem.200400409

Aldana, P.A.U., Ocampo, F., Kobl, K., Louis, B., Thibault-Starzyk, F., Daturi, M., Bazin, P., Thomas, S., Roger, A.C., 2013. Catalytic CO_2 valorization into CH_4 on Ni-based ceria-zirconia. Reaction mechanism by operando IR spectroscopy. Catal. Today 215, 201–207. https://doi.org/10.1016/j.cattod.2013.02.019

Arena, F., Frusteri, F., Parmaliana, A., Plyasova, L., Shmakov, A.N., 1996. Effect of calcination on the structure of Ni/MgO catalyst: an x-ray diffraction study (https://doi.org/DOI). J. Chem. Soc. Faraday Trans. 92, 469. https://doi.org/10.1039/ft9969200469

Arrigo, R., Logsdail, A.J., Torrente-Murciano, L., 2018. Highlights from faraday discussion on designing nanoparticle systems for catalysis, London, UK, May 2018. Chem. Commun. 54, 9385–9393. https://doi.org/10.1039/c8cc90324g

Arrigo, R., Gallarati, S., Schuster, M.E., Seymour, J.M., Gianolio, D., Silva, I., Callison, J., Feng, H., Proctor, J.E., Ferrer, P., Venturini, F., Grinter, D., Held, G., 2020. Influence of synthesis conditions on the structure of nickel nanoparticles and their reactivity in selective asymmetric hydrogenation. ChemCatChem 12, 1491–1503. https://doi.org/10.1002/cctc.201901955

Arrigo, Rosa, Blume, R., Streibel, V., Genovese, C., Roldan, A., Schuster, M.E., Ampelli, C., Perathoner, S., Velasco Vélez, J.J., Hävecker, M., Knop-Gericke, A., Schlögl, R., Centi, G., 2022. Dynamics at polarized carbon dioxide–iron oxyhydroxide interfaces unveil the origin of multicarbon product formation. ACS Catal. 12, 411–430. https://doi.org/10.1021/acscatal.1c04296

Arrigo, Rosa, Sasaki, T., Callison, J., Gianolio, D., Schuster, M.E., 2022. Monitoring dynamics of defects and single Fe atoms in N-functionalized few-layer graphene by in situ temperature programmed scanning transmission electron microscopy. J. Energy Chem. 64, 520–530. https://doi.org/10.1016/j.jechem.2021.05.005

Aziz, M.A.A., Jalil, A.A., Triwahyono, S., Mukti, R.R., Taufiq-Yap, Y.H., Sazegar, M.R., 2014. Highly active Ni-promoted mesostructured silica nanoparticles for CO_2 methanation. Appl. Catal. B-Environ. 147, 359–368. https://doi.org/10.1016/j.apcatb.2013.09.015

Aziz, M.A.A., Jalil, A.A., Triwahyono, S., Saad, M.W.A., 2015. CO_2 methanation over Ni-promoted mesostructured silica nanoparticles: Influence of Ni loading and water vapor on activity and response surface methodology studies. Chem. Eng. J. 260, 757–764. https://doi.org/10.1016/j.cej.2014.09.031

Bette, N., Thielemann, J., Schreiner, M., Mertens, F., 2016. Methanation of CO_2 over a (Mg,Al)O_x supported nickel catalyst derived from a (Ni,Mg,Al)-hydrotalcite-like precursor. ChemCatChem 8, 2903–2906. https://doi.org/10.1002/cctc.201600469

Blanco, H., Faaij, A., 2018. A review at the role of storage in energy systems with a focus on Power to Gas and long-term storage. Renew. Sustain. Energy Rev. 81, 1049–1086. https://doi.org/10.1016/j.rser.2017.07.062

Borgschulte, A., Gallandat, N., Probst, B., Suter, R., Callini, E., Ferri, D., Arroyo, Y., Erni, R., Geerlings, H., Züttel, A., 2013. Sorption enhanced CO_2 methanation. Phys. Chem. Chem. Phys. 15, 9620. https://doi.org/10.1039/c3cp51408k

Burger, T., Ewald, S., Niederdränk, A., Wagner, F.E., Köhler, K., Hinrichsen, O., 2020. Enhanced activity of co-precipitated NiFeAlO in CO_2 methanation by segregation and oxidation of Fe. Appl. Catal. A Gen. 604, 117778. https://doi.org/10.1016/j.apcata.2020.117778

Busca, G., Lorenzelli, V., 1982. Infrared spectroscopic identification of species arising from reactive adsorption of carbon oxides on metal oxide surfaces. Mater. Chem. 7, 89–126. https://doi.org/10.1016/0390-6035(82)90059-1

Centi, G., Perathoner, S., 2022a. Catalysis for an electrified chemical production. Catal. Today. https://doi.org/10.1016/j.cattod.2022.10.017

Centi, G., Perathoner, S., 2022b. Status and gaps toward fossil-free sustainable chemical production. Green. Chem. 24, 7305–7331. https://doi.org/10.1039/d2gc01572b

Climent, M.J., Corma, A., Iborra, S., Epping, K., Velty, A., 2004. Increasing the basicity and catalytic activity of hydrotalcites by different synthesis procedures. J. Catal. 225, 316–326. https://doi.org/10.1016/j.jcat.2004.04.027

Coenen, K., Gallucci, F., Mezari, B., Hensen, E., van Sint Annaland, M., 2018. An in-situ IR study on the adsorption of CO_2 and H_2O on hydrotalcites. J. CO_2 Util. 24, 228–239. https://doi.org/10.1016/j.jcou.2018.01.008

Daroughegi, R., Meshkani, F., Rezaei, M., 2021. Enhanced low-temperature activity of CO_2 methanation over ceria-promoted Ni-Al_2O_3 nanocatalyst. Chem. Eng. Sci. 230, 116194. https://doi.org/10.1016/j.ces.2020.116194

Denecke, R., Martensson, N., 2005. 4.3 Adsorbate induced surface core level shifts of metals. In: Landolt-Börnstein - Group III Condensed Matter 42A4 (Adsorbed Layers on Surfaces). Springer-Verlag, Berlin/Heidelberg, pp. 388–421. https://doi.org/10.1007/10932216_15

Di Cosimo, J.I., D\íez, V.K., Xu, M., Iglesia, E., Apestegu\ía, C.R., 1998. Structure and surface and catalytic properties of Mg-Al basic oxides. J. Catal. 178, 499–510. https://doi.org/10.1006/jcat.1998.2161

Di Cosimo, J.I., Apestegu´ıa, C.R., Ginés, M.J.L., Iglesia, E., 2000. Structural requirements and reaction pathways in condensation reactions of alcohols on Mg_yAlO_x Catalysts. J. Catal. 190, 261–275. https://doi.org/10.1006/jcat.1999.2734

Ding, M., Tu, J., Zhang, Q., Wang, M., Tsubaki, N., Wang, T., Ma, L., 2016. Enhancement of methanation of bio-syngas over CeO_2-modified Ni/Al_2O_3 catalysts. Biomass-.-. Bioenergy 85, 12–17. https://doi.org/10.1016/j.biombioe.2015.11.025

Fan, G., Li, F., Evans, D.G., Duan, X., 2014. Catalytic applications of layered double hydroxides: recent advances and perspectives. Chem. Soc. Rev. 43, 7040–7066. https://doi.org/10.1039/c4cs00160e

Feng, J., He, Y., Liu, Y., Du, Y., Li, D., 2015. Supported catalysts based on layered double hydroxides for catalytic oxidation and hydrogenation: general functionality and promising application prospects. Chem. Soc. Rev. 44, 5291–5319. https://doi.org/10.1039/c5cs00268k

Feng, J.-T., Lin, Y.-J., Evans, D.G., Duan, X., Li, D.-Q., 2009. Enhanced metal dispersion and hydrodechlorination properties of a Ni/Al_2O_3 catalyst derived from layered double hydroxides. J. Catal. 266, 351–358. https://doi.org/10.1016/j.jcat.2009.07.001

Ferreira, R.A.R., Ávila-Neto, C.N., Noronha, F.B., Hori, C.E., 2019. Study of LPG steam reform using Ni/Mg/Al hydrotalcite-type precursors. Int. J. Hydrog. Energy 44, 24471–24484. https://doi.org/10.1016/j.ijhydene.2019.07.193

Foster, M., D'Agostino, M., Passno, D., D'Agostino, M., Passno, D., 2005. Water on MgO(100) - An infrared study at ambient temperatures. Surf. Sci. 590, 31–41. https://doi.org/10.1016/j.susc.2005.06.030

Fujita, S. Ichiro, Nakamura, M., Doi, T., Takezawa, N., 1993. Mechanisms of methanation of carbon dioxide and carbon monoxide over nickel/alumina catalysts. Appl. Catal. A, Gen. 104, 87–100. https://doi.org/10.1016/0926-860X(93)80212-9

Gabrovska, M., Edreva-Kardjieva, R., Cri\csan, D., Tzvetkov, P., Shopska, M., Shtereva, I., 2011. Ni-Al layered double hydroxides as catalyst precursors for CO_2 removal by methanation. React. Kinet. Mech. Catal. 105, 79–99. https://doi.org/10.1007/s11144-011-0378-0

Garbarino, G., Riani, P., Magistri, L., Busca, G., 2014. A study of the methanation of carbon dioxide on Ni/Al_2O_3 catalysts at atmospheric pressure. Int. J. Hydrog. Energy 39, 11557–11565. https://doi.org/10.1016/j.ijhydene.2014.05.111

Garbarino, G., Kowalik Pawełand Riani, P., Antoniak-Jurak, K., Pieta, P., Lewalska-Graczyk, A., Lisowski, W., Nowakowski, R., Busca, G., Pieta, I.S., 2021. Improvement of Ni/Al2O3 catalysts for low-temperature CO_2 methanation by vanadium and calcium oxide addition. Ind. Eng. Chem. Res. 60, 6554–6564. https://doi.org/10.1021/acs.iecr.0c05556

Gazzano, M., Kagunya, W., Matteuzzi, D., Vaccari, A., 1997. Neutron diffraction studies of polycrystalline Ni/Mg/Al mixed oxides obtained from hydrotalcite-like precursors. J. Phys. Chem. B 101, 4514–4519. https://doi.org/10.1021/jp963761q

Giglio, E., Deorsola, F.A., Gruber, M., Harth, S.R., Morosanu, E.A., Trimis, D., Bensaid, S., Pirone, R., 2018. Power-to-gas through high temperature electrolysis and carbon dioxide methanation: reactor design and process modeling. Ind. Eng. Chem. Res. 57, 4007–4018. https://doi.org/10.1021/acs.iecr.8b00477

Giorgianni, G., Mebrahtu, C., Schuster, M.E., Large, A.I., Held, G., Ferrer, P., Venturini, F., Grinter, D., Palkovits, R., Perathoner, S., Centi, G., Abate, S., Arrigo, R., 2020. Elucidating the mechanism of the CO_2 methanation reaction over Ni–Fe hydrotalcite-derived catalysts via surface-sensitive in situ XPS and NEXAFS. Phys. Chem. Chem. Phys. 22, 18788–18797. https://doi.org/10.1039/D0CP00622J

González-Cortés, S.L., Aray, I., Rodulfo-Baechler, S.M.A., Lugo, C.A., Del Castillo, H.L., Loaiza-Gil, A., Imbert, F.E., Figueroa, H., Pernía, W., Rodríguez, A., Delgado, O., Casanova, R., Mendialdua, J., Rueda, F., 2007. On the structure and surface properties of $NiO/MgO\text{-}La_2O_3$ catalyst: Influence of the support composition and preparation method. J. Mater. Sci. 42, 6532–6540. https://doi.org/10.1007/s10853-007-1552-7

Götz, M., Lefebvre, J., Mörs, F., McDaniel Koch, A., Graf, F., Bajohr, S., Reimert, R., Kolb, T., Gotz, M., Lefebvre, J., Mors, F., Koch, A.M., Graf, F., Bajohr, S., Reimert, R., Kolb, T., 2016. Renewable Power-to-Gas: a technological and economic review. Renew. Energy 85, 1371–1390. https://doi.org/10.1016/j.renene.2015.07.066

Hadjiivanov, K., 2014. Identification and characterization of surface hydroxyl groups by infrared spectroscopy. In: Advances in Catalysis. Elsevier Inc, pp. 99–318. https://doi.org/10.1016/B978-0-12-800127-1.00002-3

Hakkarainen, T., Mikkola, E., Laperre, J., Gensous, F., Fardell, P., Le Tallec, Y., Baiocchi, C., Paul, K., Simonson, M., Deleu, C., Metcalfe, E., 2000. Smoke gas analysis by Fourier transform infrared spectroscopy - summary of the SAFIR project results. Fire Mater. 24, 101–112. https://doi.org/10.1002/1099-1018(200003/04)24:2<101::AID-FAM729>3.0.CO;2-2

He, L., Lin, Q., Liu, Y., Huang, Y., 2014. Unique catalysis of Ni-Al hydrotalcite derived catalyst in CO_2 methanation: cooperative effect between Ni nanoparticles and a basic support. J. Energy Chem. 23, 587–592. https://doi.org/10.1016/s2095-4956(14)60144-3

Heine, C., Lechner, B.A.J., Bluhm, H., Salmeron, M., 2016. Recycling of CO_2: probing the chemical state of the Ni(111) surface during the methanation reaction with ambient-pressure x-ray photoelectron spectroscopy. J. Am. Chem. Soc. 138, 13246–13252. https://doi.org/10.1021/jacs.6b06939

Ho, P.H., de Luna, G.S., Angelucci, S., Canciani, A., Jones, W., Decarolis, D., Ospitali, F., Aguado, E.R., Rodríguez-Castellón, E., Fornasari, G., Vaccari, A., Beale, A.M., Benito, P., 2020. Understanding structure-activity relationships in highly active La promoted Ni catalysts for CO_2 methanation. Appl. Catal. B Environ. 278, 119256. https://doi.org/10.1016/j.apcatb.2020.119256

Hussain, I., Jalil, A.A., Hassan, N.S., Hamid, M.Y.S., 2021. Recent advances in catalytic systems for CO_2 conversion to substitute natural gas (SNG): Perspective and challenges. J. Energy Chem. 62, 377–407. https://doi.org/10.1016/j.jechem.2021.03.040

Huynh, H.L., Zhu, J., Zhang, G., Shen, Y., Tucho, W.M., Ding, Y., Yu, Z., 2020. Promoting effect of Fe on supported Ni catalysts in CO_2 methanation by in situ DRIFTS and DFT study. J. Catal. 392, 266–277. https://doi.org/10.1016/j.jcat.2020.10.018

Hwang, S., Hong, U.G., Lee, J., Baik, J.H., Koh, D.J., Lim, H., Song, I.K., 2012. Methanation of carbon dioxide over mesoporous nickel–M–alumina (M = Fe, Zr, Ni, Y, and Mg) xerogel catalysts: effect of second metal. Catal. Lett. 142, 860–868. https://doi.org/10.1007/s10562-012-0842-0

Ko, J., Kim, B.-K., Han, J.W., 2016. Density functional theory study for catalytic activation and dissociation of CO_2 on bimetallic alloy surfaces. J. Phys. Chem. C. 120, 3438–3447. https://doi.org/10.1021/acs.jpcc.6b00221

Korhonen, S.T., Calatayud, M., Krause, A.O.I., 2008. Structure and stability of formates and carbonates on monoclinic zirconia: a combined study by density functional theory and infrared spectroscopy. J. Phys. Chem. C. 112, 16096–16102. https://doi.org/10.1021/jp803353v

Koschel, H., Held, G., Steinrück, H.-P., 2000. The growth of thin Cu layers on Ni(111) studied by CO titration and photoelectron spectroscopy. Surf. Sci. 453, 201–213. https://doi.org/10.1016/s0039-6028(00)00349-6

Law, Y.T., Zafeiratos, S., Neophytides, S.G., Orfanidi, A., Costa, D., Dintzer, T., Arrigo, R., Knop-Gericke, A., Schlögl, R., Savinova, E.R., 2015. In situ investigation of dissociation and migration phenomena at the Pt/electrolyte interface of an electrochemical cell. Chem. Sci. 6, 5635–5642. https://doi.org/10.1039/C5SC01421B

Lima, D., dos, S., Dias, Y.R., Perez-Lopez, O.W., 2020. CO_2 methanation over Ni-Al and Co-Al LDH-derived catalysts: the role of basicity. Sustain. Energy Fuels 4, 5747–5756. https://doi.org/10.1039/d0se01059f

Liu, J., Yu, J., Su, F., Xu, G., 2014. Intercorrelation of structure and performance of $Ni–Mg/Al_2O_3$ catalysts prepared with different methods for syngas methanation. Catal. Sci. Technol. 4, 472–481. https://doi.org/10.1039/C3CY00601H

Liu, J., Bing, W., Xue, X., Wang, F., Wang, B., He, S., Zhang, Y., Wei, M., 2016. Alkaline-assisted Ni nanocatalysts with largely enhanced low-temperature activity toward CO_2 methanation. Catal. Sci. Technol. 6, 3976–3983. https://doi.org/10.1039/C5CY02026C

Liu, K., Xu, X., Xu, J., Fang, X., Liu, L., Wang, X., 2020. The distributions of alkaline earth metal oxides and their promotional effects on Ni/CeO_2 for CO_2 methanation. J. CO_2 Util. 38, 113–124. https://doi.org/10.1016/j.jcou.2020.01.016

Liu, Q., Gao, J., Zhang, M., Li, H., Gu, F., Xu, G., Zhong, Z., Su, F., 2014. Highly active and stable Ni/γ-Al_2O_3 catalysts selectively deposited with CeO_2 for CO methanation. RSC Adv. 4, 16094–16103. https://doi.org/10.1039/C4RA00746H

Lu, B., Kawamoto, K., 2013. Preparation of the highly loaded and well-dispersed NiO/SBA-15 for methanation of producer gas. Fuel 103, 699–704. https://doi.org/10.1016/j.fuel.2012.09.009

Lucrédio, A.F., Jerkiewickz, G., Assaf, E.M., Lucredio, A.F., Jerkiewickz, G., Assaf, E.M., 2007. Nickel catalysts promoted with cerium and lanthanum to reduce carbon formation in partial oxidation of methane reactions. Appl. Catal. A Gen. 333, 90–95. https://doi.org/10.1016/j.apcata.2007.09.009

Marocco, P., Morosanu, E.A., Giglio, E., Ferrero, D., Mebrahtu, C., Lanzini, A., Abate, S., Bensaid, S., Perathoner, S., Santarelli, M., Pirone, R., Centi, G., 2018. CO_2 methanation over Ni/Al hydrotalcite-derived catalyst: experimental characterization and kinetic study. Fuel 225, 230–242. https://doi.org/10.1016/j.fuel.2018.03.137

Mathew, T., Saju, S., Raveendran, S.N., 2021. Survey of heterogeneous catalysts for the CO_2 reduction to CO via reverse water gas shift. Eng. Solut. CO_2 Convers. 281–316. https://doi.org/10.1002/9783527346523.ch12

Matteuzzi, D., Trifiro, F., Vaccari, A., Gazzano, M., Clause, O., Trifirò, F., Vaccari, A., Gazzano, M., Clause, O., 1994. Synthesis and Properties of High Surface Area Ni/Mg/Al Mixed Oxides via Anionic Clay Precursors, in: Proceedings of the International Symposium on Soft Chemistry Routes to New Materials. Trans Tech Publ, Aedermannsdorf, Switzerland, pp. 390–391. https://doi.org/10.4028/www.scientific.net/msf.152–153.391.

Mebrahtu, C., Krebs, F., Perathoner, S., Abate, S., Centi, G., Palkovits, R., 2018. Hydrotalcite based Ni-Fe/(Mg, Al)O_X catalysts for CO_2 methanation-tailoring Fe content for improved CO dissociation, basicity, and particle size. Catal. Sci. Technol. 8, 1016–1027. https://doi.org/10.1039/c7cy02099f

Mebrahtu, C., Perathoner, S., Giorgianni, G., Chen, S., Centi, G., Krebs, F., Palkovits, R., Abate, S., 2019. Deactivation mechanism of hydrotalcite-derived Ni–AlO_x catalysts during low-temperature CO_2 methanation via Ni-hydroxide formation and the role of Fe in limiting this effect. Catal. Sci. Technol. 9, 4023–4035. https://doi.org/10.1039/C9CY00744J

Mebrahtu, Chalachew, Abate, S., Chen, S., Sierra Salazar, A.F., Perathoner, S., Krebs, F., Palkovits, R., Centi, G., 2018. Enhanced catalytic activity of iron-promoted nickel on γ-Al_2O_3 nanosheets for carbon dioxide methanation. Energy Technol. 6, 1196–1207. https://doi.org/10.1002/ente.201700835

Mette, K., Kühl, S., Düdder, H., Kähler, K., Tarasov, A., Muhler, M., Behrens, M., Kuhl, S., Dudder, H., Kahler, K., Tarasov, A., Muhler, M., Behrens, M., 2014. Stable performance of Ni catalysts in the dry reforming of methane at high temperatures for the efficient conversion of CO_2 into syngas. ChemCatChem 6, 100–104. https://doi.org/10.1002/cctc.201300699

Miao, B., Ma, S.S.K., Wang, X., Su, H., Chan, S.H., 2016. Catalysis mechanisms of CO_2 and CO methanation. Catal. Sci. Technol. 6, 4048–4058. https://doi.org/10.1039/c6cy00478d

Millet, M.-M.M., Tarasov, A.V., Girgsdies, F., Algara-Siller, G., Schlögl, R., Frei, E., Schlogl, R., Frei, E., 2019. Highly dispersed $Ni^0/Ni_xMg_{1-x}O$ catalysts derived from solid solutions: how metal and support control the CO_2 hydrogenation. ACS Catal. 9, 8534–8546. https://doi.org/10.1021/acscatal.9b02332

Muroyama, H., Tsuda, Y., Asakoshi, T., Masitah, H., Okanishi, T., Matsui, T., Eguchi, K., 2016. Carbon dioxide methanation over Ni catalysts supported on various metal oxides. J. Catal. 343, 178–184. https://doi.org/10.1016/j.jcat.2016.07.018

Mustafa, A., Lougou, B.G., Shuai, Y., Wang, Z., Tan, H., 2020. Current technology development for CO_2 utilization into solar fuels and chemicals: A review. J. Energy Chem. 49, 96–123. https://doi.org/10.1016/j.jechem.2020.01.023

Mutz, B., Belimov, M., Wang, W., Sprenger, P., Serrer, M.-A., Wang, D., Pfeifer, P., Kleist, W., Grunwaldt, J.-D., 2017. Potential of an alumina-supported Ni3Fe catalyst in the methanation of CO_2: impact of alloy formation on activity and stability. ACS Catal. 7, 6802–6814. https://doi.org/10.1021/acscatal.7b01896

Navarrete, A., Centi, G., Bogaerts, A., Martin, A., York, A., Stefanidis, G.D., Martín, Á., York, A., Stefanidis, G.D., 2017. Harvesting renewable energy for carbon dioxide catalysis. Energy Technol. 5, 796–811. https://doi.org/10.1002/ente.201600609

Nematollahi, B., Rezaei, M., Lay, E.N., 2015. Selective methanation of carbon monoxide in hydrogen rich stream over Ni/CeO_2 nanocatalysts. J. Rare Earths 33, 619–628. https://doi.org/10.1016/S1002-0721(14)60462-2

Pan, Q., Peng, J., Sun, T., Gao, D., Wang, Sheng, Wang, Shudong, 2014a. CO_2 methanation on Ni/$Ce_{0.5}Zr_{0.5}O_2$ catalysts for the production of synthetic natural gas. Fuel Process. Technol. 123, 166–171. https://doi.org/10.1016/j.fuproc.2014.01.004

Pan, Q., Peng, J., Sun, T., Wang, Sheng, Wang, Shudong, 2014b. Insight into the reaction route of CO_2 methanation: promotion effect of medium basic sites. Catal. Commun. 45, 74–78. https://doi.org/10.1016/j.catcom.2013.10.034

Papadopoulos, P., 2008. Friedrich siebert and peter hildebrandt, vibrational spectroscopy in life science. 487–487. Colloid Polym. Sci. 286. https://doi.org/10.1007/s00396-007-1816-4

Papanikolaou, G., Centi, G., Perathoner, S., Lanzafame, P., 2022a. Catalysis for e-chemistry: need and gaps for a future de-fossilized chemical production, with focus on the role of complex (Direct) syntheses by electrocatalysis. ACS Catal. 12, 2861–2876. https://doi.org/10.1021/acscatal.2c00099

Papanikolaou, G., Centi, G., Perathoner, S., Lanzafame, P., 2022b. Transforming catalysis to produce e-fuels: prospects and gaps. Chin. J. Catal. 43, 1194–1203. https://doi.org/10.1016/s1872-2067(21)64016-0

Parmaliana, A., Arena, F., Frusteri, F., Giordano, N., 1990. Temperature-programmed reduction study of NiO-MgO interactions in magnesia-supported Ni catalysts and NiO-MgO physical mixture. J. Chem. Soc., Faraday Trans. 86, 2663–2669. https://doi.org/10.1039/ft9908602663

Perathoner, S., Van Geem, K.M., Marin, G.B., Centi, G., 2021. Reuse of CO_2 in energy intensive process industries. Chem. Commun. 57, 10967–10982. https://doi.org/10.1039/d1cc03154f

Price, C.A.H., Reina, T.R., Liu, J., 2021. Engineering heterogenous catalysts for chemical CO_2 utilization: lessons from thermal catalysis and advantages of yolk@shell structured nanoreactors. J. Energy Chem. 57, 304–324. https://doi.org/10.1016/j.jechem.2020.08.061

Rebours, B., d'Espinose de la Caillerie, J.-B., Clause, O., Delacaillerie, J.B.D., Clause, O., 1994. Decoration of nickel and magnesium-oxide crystallites with spinel-type phases (https://doi.org/DOI). J. Am. Chem. Soc. 116, 1707–1717. https://doi.org/10.1021/ja00084a011

Salmeron, M., Schlogl, R., 2008. Ambient pressure photoelectron spectroscopy: a new tool for surface science and nanotechnology. Surf. Sci. Rep. 63, 169–199. https://doi.org/10.1016/j.surfrep.2008.01.001

Salomone, F., Giglio, E., Ferrero, D., Santarelli, M., Pirone, R., Bensaid, S., 2019. Techno-economic modelling of a Power-to-Gas system based on SOEC electrolysis and CO_2 methanation in a RES-based electric grid. Chem. Eng. J. 377, 120233. https://doi.org/10.1016/j.cej.2018.10.170

Serrer, M., Stehle, M., Schulte, M.L., Besser, H., Pfleging, W., Saraçi, E., Grunwaldt, J., 2021. Spatially-resolved insights into local activity and structure of Ni-Based CO_2 methanation catalysts in fixed-bed reactors. ChemCatChem 13, 3010–3020. https://doi.org/10.1002/cctc.202100490

Silva, C.C.C.M., Ribeiro, N.F.P., Souza, M.M.V.M., Aranda, D.A.G., 2010. Biodiesel production from soybean oil and methanol using hydrotalcites as catalyst. Fuel Process. Technol. 91, 205–210. https://doi.org/10.1016/j.fuproc.2009.09.019

Su, X., Xu, J., Liang, B., Duan, H., Hou, B., Huang, Y., 2016. Catalytic carbon dioxide hydrogenation to methane: a review of recent studies. J. Energy Chem. 25, 553–565. https://doi.org/10.1016/j.jechem.2016.03.009

Summa, P., Świrk, K., Wierzbicki, D., Motak, M., Alxneit, I., Rønning, M., Da Costa, P., 2021. Co-precipitated Ni-Mg-Al hydrotalcite-derived catalyst promoted with vanadium for CO_2 methanation. Molecules 26, 6506. https://doi.org/10.3390/molecules26216506

Summa, P., Samojeden, B., Motak, M., Wierzbicki, D., Alxneit, I., Świerczek, K., Da Costa, P., 2022. Investigation of Cu promotion effect on hydrotalcite-based nickel catalyst for CO_2 methanation. Catal. Today 384–386, 133–145. https://doi.org/10.1016/j.cattod.2021.05.004

Sun, C., Świrk, K., Wierzbicki, D., Motak, M., Grzybek, T., Da Costa, P., 2021. On the effect of yttrium promotion on Ni-layered double hydroxides-derived catalysts for hydrogenation of CO_2 to methane. Int. J. Hydrog. Energy 46, 12169–12179. https://doi.org/10.1016/j.ijhydene.2020.03.202

Tada, S., Nagase, H., Fujiwara, N., Kikuchi, R., 2021. What are the best active sites for CO_2 methanation over Ni/CeO_2? Energy Fuels 35, 5241–5251. https://doi.org/10.1021/acs.energyfuels.0c04238

Torrente-Murciano, L., 2016. The importance of particle-support interaction on particle size determination by gas chemisorption. J. Nanopart. Res. 18, 1–7. https://doi.org/10.1007/s11051-016-3385-2

Tsiotsias, A.I., Charisiou, N.D., AlKhoori, A., Gaber, S., Stolojan, V., Sebastian, V., van der Linden, B., Bansode, A., Hinder, S.J., Baker, M.A., Polychronopoulou, K., Goula, M.A., 2022. Optimizing the oxide support composition in Pr-doped CeO_2 towards highly active and selective Ni-based CO_2 methanation catalysts. J. Energy Chem. 71, 547–561. https://doi.org/10.1016/j.jechem.2022.04.003

Vaccari, A., 1998. Preparation and catalytic properties of cationic and anionic clays (https://doi.org/Doi). Catal. Today 41, 53–71. https://doi.org/10.1016/S0920-5861(98)00038-8

Veloso, C.O., Pérez, C.N., de Souza, B.M., Lima, E.C., Dias, A.G., Monteiro, J.L.F., Henriques, C.A., 2008. Condensation of glyceraldehyde acetonide with ethyl acetoacetate over Mg,Al-mixed oxides derived from hydrotalcites. Microporous Mesoporous Mater. 107, 23–30. https://doi.org/10.1016/j.micromeso.2007.05.036

Vogt, C., Groeneveld, E., Kamsma, G., Nachtegaal, M., Lu, L., Kiely, C.J., Berben, P.H., Meirer, F., Weckhuysen, B.M., 2018. Unravelling structure sensitivity in CO_2 hydrogenation over nickel. Nat. Catal. 1, 127–134. https://doi.org/10.1038/s41929-017-0016-y

Vogt, C., Monai, M., Kramer, G.J., Weckhuysen, B.M., 2019. The renaissance of the Sabatier reaction and its applications on Earth and in space. Nat. Catal. 2, 188–197. https://doi.org/10.1038/s41929-019-0244-4

Völs, P., Hilbert, S., Störr, B., Bette, N., Lißner, A., Seidel, J., Mertens, F., 2021. Methanation of CO_2 and CO by (Ni,Mg,Al)-hydrotalcite-derived and related catalysts with varied magnesium and aluminum oxide contents. Ind. Eng. Chem. Res. 60, 5114–5123. https://doi.org/10.1021/acs.iecr.1c00028

Wang, Q., O'Hare, D., O'Hare, D., 2012. Recent advances in the synthesis and application of layered double hydroxide (LDH) nanosheets. Chem. Rev. 112, 4124–4155. https://doi.org/10.1021/cr200434v

Wang, Q., Gao, Y., Tumurbaatar, C., Bold, T., Wei, F., Dai, Y., Yang, Y., 2022. Tuned selectivity and enhanced activity of CO_2 methanation over Ru catalysts by modified metal-carbonate interfaces. J. Energy Chem. 64, 38–46. https://doi.org/10.1016/j.jechem.2021.04.039

Wang, Q.A., Tay, H.H., Ng, D.J.W., Chen, L.W., Liu, Y., Chang, J., Zhong, Z.Y., Luo, J.Z., Borgna, A., 2010. The effect of trivalent cations on the performance of Mg-M-CO_3 layered double hydroxides for high-temperature CO_2 capture. ChemSusChem 3, 965–973. https://doi.org/10.1002/cssc.201000099

Wang, T., Ma, H., Zeng, L., Li, D., Tian, H., Xiao, S., Gong, J., 2016. Highly loaded Ni-based catalysts for low temperature ethanol steam reforming. Nanoscale 8, 10177–10187. https://doi.org/10.1039/c6nr02586b

Wei, M., Fu, Q., Yang, Y., Wei, W., Crumlin, E., Bluhm, H., Bao, X., 2015. Modulation of surface chemistry of CO on Ni(111) by surface graphene and carbidic carbon. J. Phys. Chem. C. 119, 13590–13597. https://doi.org/10.1021/acs.jpcc.5b01395

Wierzbicki, D., Baran Rafałand D\kebek, R., Motak, M., Grzybek, T., Gálvez, M.E., Da Costa, P., 2017. The influence of nickel content on the performance of hydrotalcite-derived catalysts in CO_2 methanation reaction. Int. J. Hydrog. Energy 42, 23548–23555. https://doi.org/10.1016/j.ijhydene.2017.02.148

Wierzbicki, D., Baran, R., Dębek, R., Motak, M., Gálvez, M.E., Grzybek, T., Da Costa, P., Glatzel, P., 2018. Examination of the influence of La promotion on Ni state in hydrotalcite-derived catalysts under CO_2 methanation reaction conditions: operando X-ray absorption and emission spectroscopy investigation. Appl. Catal. B Environ. 232, 409–419. https://doi.org/10.1016/j.apcatb.2018.03.089

Winter, L.R., Gomez, E., Yan, B.H., Yao, S.Y., Chen, J.G.G., 2018. Tuning Ni-catalyzed CO_2 hydrogenation selectivity via Ni-ceria support interactions and Ni-Fe bimetallic formation. Appl. Catal. B-Environ. 224, 442–450. https://doi.org/10.1016/j.apcatb.2017.10.036

Xiao, X., Wang, J., Li, J., Dai, H., Jing, F., Liu, Y., Chu, W., 2021. Enhanced low-temperature catalytic performance in CO_2 hydrogenation over Mn-promoted NiMgAl catalysts derived from quaternary hydrotalcite-like compounds. Int. J. Hydrog. Energy 46, 33107–33119. https://doi.org/10.1016/j.ijhydene.2021.07.163

Xu, L., Wang, F., Chen, M., Yang, H., Nie, D., Qi, L., Lian, X., 2017. Alkaline-promoted Ni based ordered mesoporous catalysts with enhanced low-temperature catalytic activity toward CO_2 methanation. RSC Adv. 7, 18199–18210. https://doi.org/10.1039/c7ra01673e

Xu, Z., Wang, N., Chu, W., Deng, J., Luo, S., 2015. In situ controllable assembly of layered-double-hydroxide-based nickel nanocatalysts for carbon dioxide reforming of methane. Catal. Sci. Technol. 5, 1588–1597. https://doi.org/10.1039/c4cy01302f

Yan, B., Zhao, B., Kattel, S., Wu, Q., Yao, S., Su, D., Chen, J.G., 2019. Tuning CO_2 hydrogenation selectivity via metal-oxide interfacial sites. J. Catal. 374, 60–71. https://doi.org/10.1016/j.jcat.2019.04.036

Yang Lim, J., McGregor, J., Sederman, A.J., Dennis, J.S., 2016. Kinetic studies of CO_2 methanation over a Ni/γ-Al_2O_3 catalyst using a batch reactor. Chem. Eng. Sci. 141, 28–45. https://doi.org/10.1016/j.ces.2015.10.026

Ye, Y., Yang, H., Qian, J., Su, H., Lee, K.-J., Cheng, T., Xiao, H., Yano, J., Goddard, W.A., Crumlin, E.J., Goddard William 3rd, A., Crumlin, E.J., 2019. Dramatic differences in carbon dioxide adsorption and initial steps of reduction between silver and copper. Nat. Commun. 10, 1875. https://doi.org/10.1038/s41467-019-09846-y

Younas, M., Loong Kong, L., Bashir, M.J.K., Nadeem, H., Shehzad, A., Sethupathi, S., 2016. Recent advancements, fundamental challenges, and opportunities in catalytic methanation of CO_2. Energy Fuels 30, 8815–8831. https://doi.org/10.1021/acs.energyfuels.6b01723

Yuan, K., Zhong, J.-Q., Zhou, X., Xu, L., Bergman, S.L., Wu, K., Xu, G.Q., Bernasek, S.L., Li, H.X., Chen, W., 2016. Dynamic oxygen

on surface: catalytic intermediate and coking barrier in the modeled CO_2 reforming of CH_4 on Ni (111). ACS Catal. 6, 4330–4339. https://doi.org/10.1021/acscatal.6b00357

Zamani, A.H., Ali, R., Abu Bakar, W.A.W., 2015. Optimization of CO_2 methanation reaction over M*/Mn/Cu–Al_2O_3 (M*: Pd, Rh and Ru) catalysts. J. Ind. Eng. Chem. 29, 238–248. https://doi.org/10.1016/j.jiec.2015.02.028

Zhao, M.-Q., Zhang, Q., Zhang, W., Huang, J.-Q., Zhang, Y., Su, D.S., Wei, F., 2010. Embedded high density metal nanoparticles with extraordinary thermal stability derived from guest–host mediated layered double hydroxides. J. Am. Chem. Soc. 132, 14739–14741. https://doi.org/10.1021/ja106421g

Zhou, R., Rui, N., Fan, Z.G., Liu, C.J., 2016. Effect of the structure of Ni/TiO_2 catalyst on CO_2 methanation. Int. J. Hydrog. Energy 41, 22017–22025. https://doi.org/10.1016/j.ijhydene.2016.08.093

Zhu, Y., Zhang, S., Chen, B., Zhang, Z., Shi, C., 2016. Effect of Mg/Al ratio of NiMgAl mixed oxide catalyst derived from hydrotalcite for carbon dioxide reforming of methane. Catal. Today 264, 163–170. https://doi.org/10.1016/j.cattod.2015.07.037